
Article:
Fougere, D., Dolan, J., Rhodes, E. et al. (2024) Refined Holocene slip rate for the western and central segments of the Garlock fault: record of alternating millennial-scale periods of fast and flow fault slip. Seismica, 3 (2). ISSN: 2816-9387

https://doi.org/10.26443/seismica.v3i2.1202

---

doi:10.26443/seismica.v3i2.1202

Refined Holocene Slip Rate for the Western and Central Segments of the Garlock Fault: Record of Alternating Millennial-Scale Periods of Fast and Slow Fault Slip

Dannielle M. Fougere *[1], **James F. Dolan** [1], **Edward J. Rhodes** [2], **Sally F. McGill** [3]

[1]Department of Earth Sciences, University of Southern California, Los Angeles, CA 90089, USA, [2]Department of Geography, University of Sheffield, Sheffield, S10 2TN, UK, [3]Department of Geological Sciences, California State University San Bernardino, San Bernardino, CA 92407, USA

Author contributions: *Conceptualization*: D. M. Fougere, J. F. Dolan, E. J. Rhodes, S. F. McGill. *Data Curation*: J. F. Dolan, E. J. Rhodes, S. F. McGill. *Formal Analysis*: D. M. Fougere, E. J. Rhodes. *Funding Acquisition*: J. F. Dolan, E. J. Rhodes, S. F. McGill. *Investigation*: D. M. Fougere, J. F. Dolan, E. J. Rhodes, S. F. McGill. *Methodology*: D. M. Fougere, J. F. Dolan, E. J. Rhodes, S. F. McGill. *Project Administration*: D. M. Fougere, J. F. Dolan, E. J. Rhodes, S. F. McGill. *Resources*: D. M. Fougere, J. F. Dolan, E. J. Rhodes, S. F. McGill. *Software*: D. M. Fougere. *Supervision*: J. F. Dolan. *Validation*: D. M. Fougere. *Visualization*: D. M. Fougere, S. F. McGill. *Writing – original draft*: D. M. Fougere. *Writing – review & editing*: J. F. Dolan, E. J. Rhodes, S. F. McGill.

Abstract We use lidar- and field-based mapping coupled with single-grain infrared-stimulated luminescence dating to constrain three new slip rate estimates from the western and central segments of the Garlock fault in southern California, revealing a more complete picture of incremental slip rate in time and space for this major plate-boundary fault. These new rates reinforce and refine previous evidence showing that the Garlock fault experiences significant temporal variations in slip rates that span multiple earthquake cycles, with multi-millennial periods of very fast (13-14 mm/yr) early and late Holocene slip separated by a mid-Holocene period of slow slip (3 mm/yr). Similar ca. 8 ka slip rates for the central Garlock fault of 8.8 ± 1.0 mm/yr and 8.2 +1.0/-0.8 mm/yr for the western Garlock fault demonstrate that the fault has slipped at a faster long-term average rate than suggested by previous studies. These fast rates are consistent with kinematic models in which the western and central Garlock fault segments are driven primarily by lateral extrusion associated with N-S contractional shortening, with additional slip driven by WNW-ENE Basin and Range extension north of the fault and minor rotation of the Garlock within the N-S zone of dextral ECSZ shear.

Non-technical summary Advanced geomorphic mapping and dating methods allow us to study the Garlock fault in southern California. Past research has shown that some major faults show irregular behavior over thousand-year time scales. Specifically, our findings show that during some periods the Garlock fault has been slipping faster than its long-term average rate, and at other times this fault has been slipping slower than its long-term average rate. These new insights build onto existing data and allow scientists to better understand complex behaviors seen in fault networks, ultimately, better informing seismic hazard assessments.

Production Editor:
Gareth Funning
Handling Editor:
Randolph Williams
Copy & Layout Editor:
Hannah F. Mark

Signed reviewer(s):
Jonathan Griffin

Received:
January 28, 2024
Accepted:
June 6, 2024
Published:
July 5, 2024

1 Introduction

Documenting patterns of elastic strain accumulation and release through time and space on major faults is of fundamental importance for understanding the mechanisms governing the behavior of plate boundary fault systems and assessing the associated seismic hazard. Increasingly detailed slip records suggest that some faults display relatively constant slip rates through time (e.g., Berryman et al., 2012; Noriega et al., 2006; Salisbury et al., 2018; Gold et al., 2011; Kozacı et al., 2009), whereas others experience significant temporal variations in slip rates over multiple earthquake cycles (e.g., Wallace, 1987; Friedrich et al., 2004; Weldon et al., 2004; Dolan et al., 2007, 2016; Ninis et al., 2013; Onderdonk et al., 2015; Zinke et al., 2017, 2019, 2021; Hatem et al., 2020; Gold and Cowgill, 2011). Incremental slip rate records from major faults provide insights into the constancy (or non-constancy) of fault slip through time, constraining temporal and displacement scales over which some faults exhibit non-constant behavior. This information, in turn, provides constraints on what mechanisms may be controlling this behavior. Yet, the underlying mechanisms modulating these behaviors are not well understood. One reason for this is that this discussion remains highly data-limited – there are still too few detailed incremental slip rate records developed from hybrid studies that combine both earthquake timings and displacements to develop a true "dated path" of slip.

The key to understanding the mechanisms driving slip rate variability lies in first documenting patterns of fault slip through time and space on major plate boundary faults. Generating a rich incremental slip rate data set records the phenomenology of time-variable fault slip, and permits a comprehensive assessment of patterns of strain release through time and space. Such

*Corresponding author: dfougere@usc.edu

data provide key constraints on insights into the physical mechanisms modulating variations in slip behavior observed on major faults, such as the Garlock fault discussed in this study. Moreover, geologic slip rates are used as fundamental inputs in probabilistic seismic hazard assessment (PSHA) models, which often disregard temporal variability over long (i.e., multi-millennia) time periods (e.g., Field et al., 2015, 2017). New incremental slip rates such as those presented here will thus help to advance our understanding of the use of geologic slip rates for the development of the next generation of PSHA models (e.g., Van Dissen et al., 2020).

In this paper, we present three new and refined mid-to-early-Holocene slip rates from the central and western Garlock fault. These slip rates add to the emerging incremental slip rate record of the Garlock fault, notably helping to resolve the sparse record during mid- to early Holocene time. We discuss these results in light of their implications for alternating millennial-scale periods of fast and slow fault slip on the Garlock fault as well as for system-level behavior of the plate boundary fault system in southern California.

2 The Garlock Fault

The Garlock fault is a major left-lateral strike-slip fault that extends eastward from its intersection with the San Andreas fault for 250 km to southern Death Valley (Figure 1). It forms a prominent physiographic boundary between the E-W extension of the Basin and Range Province to the north and the non-extending Mojave block to the south (Davis and Burchfiel, 1973). Cumulative displacement along the Garlock fault is recorded as 48-64 km since fault initiation (Monastero et al., 1997; Smith, 1962; Smith and Ketner, 1970; Davis and Burchfiel, 1973), which occurred between 17 and 10 Ma (Andrew et al., 2014; Burbank and Whistler, 1987; Monastero et al., 1997; Loomis and Burbank, 1988), and likely at ca. 11 Ma (Blythe and Longinotti, 2013; Andrew et al., 2014). The Garlock fault has been divided into three segments defined by changes in strike and structural complexities. Specifically, a two-to-three-km-wide step-over at Koehn Lake between the western and central segments coincides with a 10° change in strike, and a 15° change in strike near the Quail Mountains between the central and eastern segments (McGill and Sieh, 1991). The E-W Garlock fault is embedded sub-perpendicular to Pacific-North American plate boundary motion within a zone of N-NW-trending dextral shear known as the Eastern California shear zone (ECSZ). The central and eastern segments of the Garlock fault lie within the ECSZ, but the western fault segment lies to the west of this zone of dextral shear.

2.1 Previous Studies

Although the Garlock fault displays abundant geomorphic evidence for past earthquakes, it has not generated any large ground-rupturing earthquakes during the historic period (McGill and Sieh, 1991, 1993; Dawson et al., 2003; McGill et al., 2009; Ganev et al., 2012; Madden Madugo et al., 2012; Rittase et al., 2014; Dolan et al., 2016). Several paleoseismic investigations, however, have documented evidence for large-magnitude (Mw > 7.2) Holocene earthquakes along the western and central segments of the Garlock fault (McGill and Sieh, 1991; McGill, 1992; McGill and Rockwell, 1998; Dawson et al., 2003; McGill et al., 2009; Madden Madugo et al., 2012; Pena, 2019). Additionally, the western and central segments exhibit relatively fast slip rates, with several studies recording latest-Pleistocene to early-Holocene rates of 5 to 8 mm/yr (Clark and Lajoie, 1974; Ganev et al., 2012; McGill and Sieh, 1993; McGill et al., 2009), which are comparable to longer-term rates averaged over million-year time scales (Burbank and Whistler, 1987; Carter, 1994; Monastero et al., 1997; Loomis and Burbank, 1988).

On the western segment of the Garlock fault at Clark Wash (Figure 1), McGill et al. (2009) documented a 66 ± 6 m offset of an older alluvial fan into which Clark Wash has subsequently incised. They determined this offset by back-slipping the riser (i.e., stream bank) between the older fan surface and the top surface of the younger incised channel deposits until they achieved a sedimentologically plausible configuration. Eight detrital charcoal ages collected from the deepest exposed deposits of the younger channel fill in a fault-parallel trench all yielded similar early Holocene calibrated radiocarbon ages of 7.7-8.1 ka (McGill et al., 2009). The older fan deposits into which Clark Wash incised contained a detrital charcoal sample representing a maximum-possible age of fan abandonment at this site of 13.3 ka, indicating Clark Wash incision occurred between ca. 8.0 ka and 13.3 ka. Consequently, McGill et al. (2009) used an age of 9.3 +4.0/-1.2 ka as the preferred age of Clark Wash incision and subsequent offset, with this age based on the correlation of climatically driven pulses of alluvial fan deposition within the Mojave Desert during the 8.0-13.3 ka range allowed by the radiocarbon dates (Harvey and Wells, 2003). Combining the 9.3 +4.0/-1.2 ka preferred age and 66 ± 6 m offset yielded a broad potential slip rate of 7.6 +3.1/-2.3 mm/yr slip rate averaged over Holocene to latest Pleistocene time (McGill et al., 2009).

Along the westernmost part of the central segment of the Garlock fault, 30 km west of Summit Range West, Clark and Lajoie (1974) documented a slip rate from a site on the northeast corner of Koehn Lake (Figure 1) by combining a ~75 m berm offset (Clark, 1973) with radiocarbon-dated berm-crest lacustrine tufa deposits yielding a slip rate of 4.5-6.1 mm/yr (after Ganev et al., 2012) (application of dendrochronological calibration to the uncalibrated radiocarbon dates reported in Clark and Lajoie, 1974). This slip rate is considered a minimum since the tufa was deposited before offset of the berm began.

Thirty kilometers farther east, Ganev et al. (2012) documented a slip rate along the central segment at what we refer to as the Summit Range West site of 5.3 +1.0/-2.5 mm/yr based on the 70-m offset of a well-defined, incised edge of an alluvial fan and a 10Be cosmogenic radionuclide depth profile age of the fan surface of 13.3 +5.9/-1.1 ka. Ganev et al. (2012) suggested two additional potential slip rate estimates at the Summit Range West site based on a 58 m offset of the deeply incised

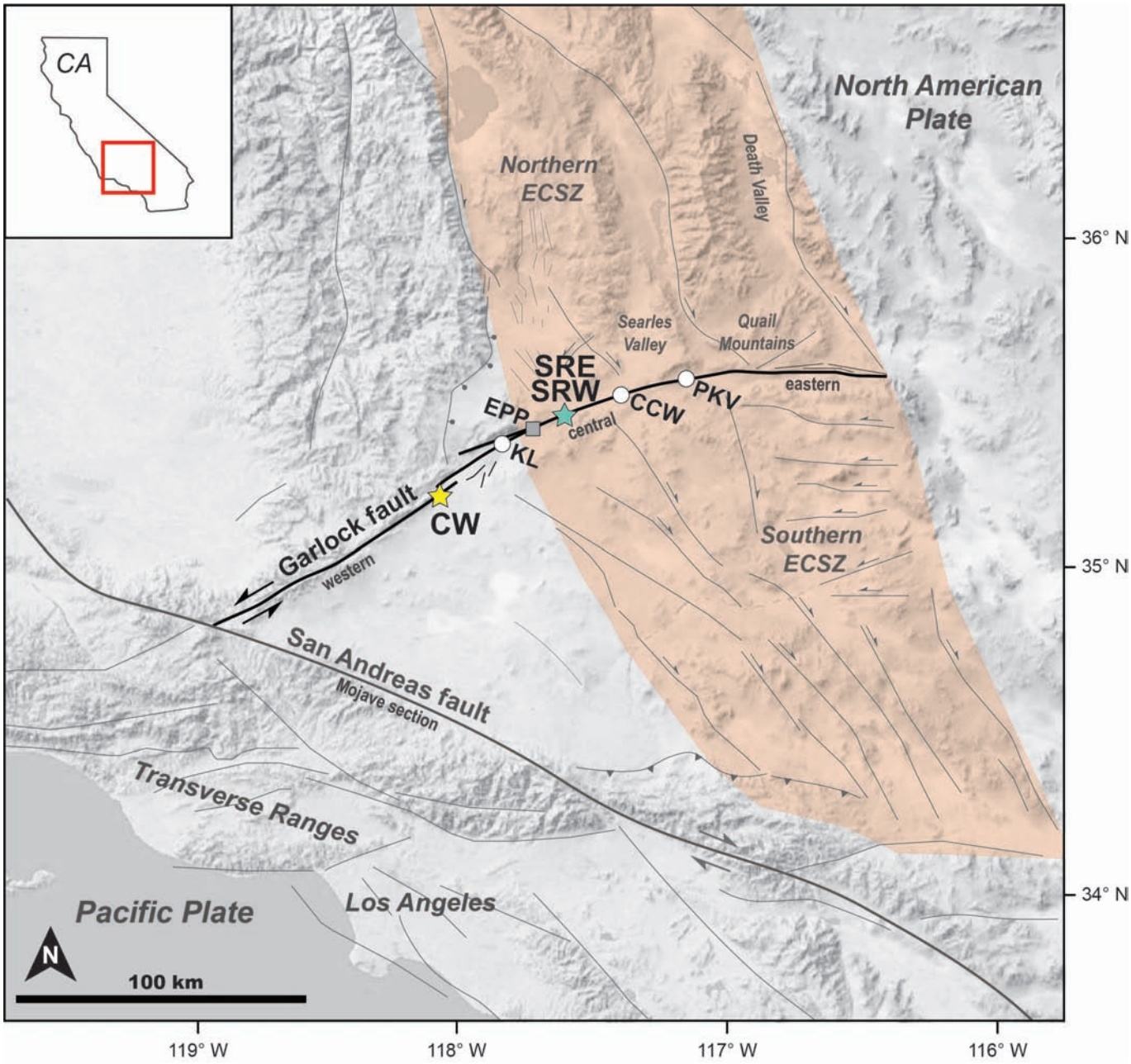

Figure 1 Map of the Garlock fault and other active faults around the Mojave region of southern California (gray), including the Mojave section of the San Andreas fault. Yellow star is the location of the Clark Wash (CW) site of this study, blue star is the location of the Summit Range West (SRW) and Summit Range East (SRE) sites of this study. White circles show the locations of past slip rate studies; CCW is the Christmas Canyon West site of Dolan et al. (2016), KL is the Koehn Lake site of Clark and Lajoie (1974), and PKV is the Pilot Knob Valley site of Rittase et al. (2014). A gray square shows the location of the El Paso Peaks (EPP) paleoseismic site of Dawson et al. (2003). Quaternary fault traces sourced from US Geological Survey and California Geological Survey (2023).

stream thalweg. Possible ages of thalweg incision were inferred to correspond to significant climate changes in the southwestern United States, one change which occurred at the end of the Younger Dryas (~11.5 ka) resulted in a more humid climate, and another at 8-10 ka that marked the onset of summer monsoonal rainfall patterns, providing estimated slip rates of 5.1 ± 0.3 mm/yr and 6.6 ± 1.2 mm/yr, respectively. In this paper, we refine both the Clark Wash (McGill et al., 2009) and Summit Range West (Ganev et al., 2012) slip rates using newly collected luminescence age data, and we present a new slip rate for the Summit Range East site, located 3 km east of the Summit Range West site.

Although these earlier studies reveal relatively similar long-term slip rates averaged over latest Pleistocene and early Holocene time of ~5-8 mm/yr, recent studies suggest that the Garlock fault slip rate has been highly irregular during the Holocene. For example, Dolan et al. (2016) documented an accelerated, late Holocene slip rate of >14 +2.2/-1.8 mm/yr from a series of 1.9 ka alluvial fans that have been offset by ~26 m at the Christmas Canyon West site (~15 km east of Summit Range West), at least 2-3x faster than the long-term average rate. Similarly, Rittase et al. (2014) also documented

an accelerated, late Holocene slip rate of 10.8 to 12.5 mm/yr from a shutter ridge at the Pilot Knob Valley site (Figure 1). Age constraints were based on soil development and one optically stimulated luminescence age from deposits that may correlate with those of the buttressing shutter ridge. Notably, the fast late-Holocene rate at Christmas Canyon West appears to coincide with a cluster of four earthquakes recorded on the central segment that occurred between ca. 0.5 and 2 ka at the El Paso Peaks site (Figure 1, Dawson et al., 2003). The fast late-Holocene rate in Pilot Knob Valley of Rittase et al. (2014) also includes that period but may include slip accumulated between ~ 3.5 ka and ~ 0.5 ka.

3 New Slip Rate Data from the Central and Western Garlock Fault

In order to refine the current incremental slip rate record (i.e., by calculating new slip rates) for the western and central Garlock fault, we use field mapping and analysis of high-resolution (0.5 m) GeoEarthScope lidar data collected along the Garlock fault (data available at www.opentopography.org) to accurately measure tectonically offset geomorphic features, combined with age estimates using post-IR infrared stimulated luminescence (post-IR IRSL225) protocol (Rhodes, 2015) and radiocarbon dating of detrital charcoal. We document three mid-to-early-Holocene slip rates from (1) the Summit Range East site, a new slip rate for the central Garlock fault; (2) the Summit Range West site, a refined slip rate for the central Garlock fault, following earlier work by Ganev et al. (2012); and (3) the Clark Wash site, a refined slip rate from the western Garlock fault following on from the study of McGill et al. (2009). The addition of new post-IR IRSL225 data for the Summit Range West and Clark Wash sites significantly narrows the slip rate ranges at both of the latter sites.

3.1 Summit Range East

The Summit Range East (SRE) site is located on the north-facing mountain front of the Summit Range on the central segment of the Garlock fault, ~3 km east of the Ganev et al. (2012) Summit Range West site (Figure 2). The Garlock fault is particularly well-defined in the geomorphology along this stretch of the fault. High-resolution lidar data reveal a narrow, linear fault trace with numerous well-defined left-lateral offsets of northward-flowing streams and associated alluvial fans.

At the SRE site, the alluvial fan of interest, Qfc2, and its associated distributary fan channels have been offset left-laterally by the Garlock fault (Figure 3a). Analysis of topographic profiles derived from lidar data measured perpendicular to flow direction across alluvial fans Qfc1 and Qfc2 reveal a classic convex-up morphology, suggesting that they might be the same fan, and that difference in fine-scale surface morphology may be due to enhanced erosion of Qfc1 on the western edge of this fan system. At this site, the alluvial fan of interest, Qfc2, and its associated distributary fan channels have been offset left-laterally by the Garlock fault (Figure 3a).

Whether Qfc1 and Qfc2 are actually different-aged fans does not affect our slip rate determination based on the restorations of Channel 1 (Ch-1) and Channel 2 (Ch-2). Alluvium at this site was sourced from Mesozoic granites exposed in the Summit Range, south of the fault, and has been transported northwards across the fault towards Searles Valley. On its eastern edge, the depositional edge of the Qfc2 fan atop Mesozoic bedrock is exposed south of the fault. Two northeastward-flowing channels (Ch-2 and Channel 3 [Ch-3]) have incised into the southeastern edge of the Qfc2 fan and were subsequently offset by the fault. The modern channel extending through the study site (Ch-0) has incised into the northwestern edge of the Qfc1 and Qfc2 fans.

3.1.1 Offset Measurements

The fault offset at the SRE site is based on the restoration of (1) a prominent distributary channel incised into the Qfc2 surface (Ch-1 in Figure 3a), and (2) one of the northeastward-flowing offset drainages incised into the southeastern edge of Qfc2 (Ch-2 in Figure 3a). Offset measurements were determined by incrementally back-slipping one side of the fault relative to the other to determine the minimum-possible, preferred, and maximum-possible offset values. Maximum- and minimum-possible offset uncertainty limits were determined by progressively back-slipping the fault in 50 cm increments until a point was reached where the restored geomorphic features were no longer in a sedimentologically plausible configuration (see Figure S1).

Using these criteria, we measured independent offset estimates for Ch-1 and the largest offset Ch-2 where our reported uncertainties represent the maximum and minimum limits of sedimentologically allowable geometries. Ch-1 yielded a preferred offset measurement of 38 ± 1 m (Figure 3b and c). This tight error constraint was determined by a pronounced bend of Ch-1 at the fault crossing at restorations smaller than 37 m and larger than 39 m. Ch-2 yielded an offset measurement of 40 ± 3 m. The minimum estimate was determined on the basis that restorations smaller than 37 m would have shut off the downstream segment of the incised channel from its upstream equivalent, beheading the channel at the fault trace. The maximum estimate was determined by the incised channel forming a prominent "s-bend" across the fault at restorations larger than 43 m. The width of the channel, post-offset modification of topography slightly north of the fault, and the oblique orientation of the channel with respect to the fault result in slightly larger error bounds for Ch-2 than for the sharply defined Ch-1 incised into the Qfc2 surface. Therefore, in the following slip rate calculations, we used the tightly constrained prominent distributary channel offset of 38 ± 1 m as our preferred displacement value. The independent offset for Ch-2 may be slightly larger than Ch-1, however, the measurements of 38 ± 1 m and 40 ± 3 m for these two channels overlap within error. An additional channel (Ch-3b), located 15 m west of and adjacent to the 40 ± 3 m offset channel, has also incised into the southeastern edge of the Qfc2 fan south of the fault. Reconstructing Ch3-b with Ch-2a reveals that this feature

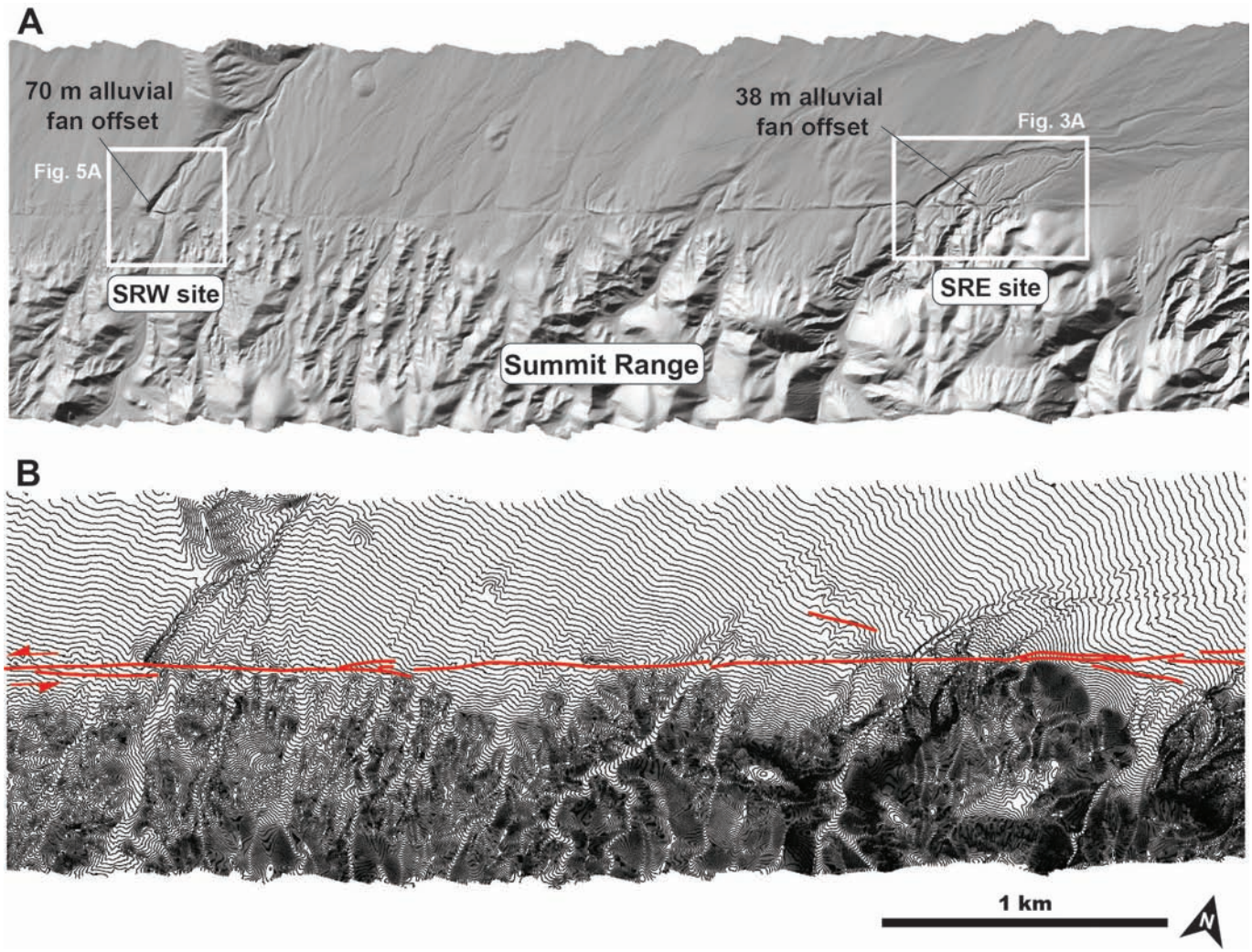

Figure 2 (a) Annotated lidar-derived hillshade of the Summit Range West (SRW) study site originally studied by Ganev et al. (2012) at N 35.479116° W 117.560319°, and the Summit Range East (SRE) at N 35.485943° W 117.530138°. (b) Topographic map (2-m contour interval) derived from the lidar dataset of the same areas as in (a). Garlock fault trace shown by the red line.

is likely a result of a younger incision event following the accumulation of ~15 to 20 m of left-lateral fault slip after deposition of Qfc2 ceased. We, therefore, do not consider this offset in the slip rate calculation.

3.1.2 Age Constraints

We use the post-IR IRSL225 single-grain potassium feldspar luminescence dating method of Rhodes (2015) to determine the age of Qfc2 alluvial fan deposition, a detailed description of this protocol for all three sites discussed in this paper can be found in Supplementary Material 3. This protocol has already been successfully applied to dating sites on the central Garlock fault (e.g., Rhodes, 2015; Dolan et al., 2016) and at other sites in southern California (e.g., Del Vecchio et al., 2018; Kirby et al., 2018; Saha et al., 2021). We hand-excavated a 1.5-m-deep by 1-m-square pit (N 35.486133°, W 117.529533°, at an elevation of 854 m) into the Qfc2 fan surface and collected four IRSL samples in steel tubes from sand-rich horizons in a vertical sequence at depths between 25-95 cm (Figure 4a). The sediments exposed in the pit consist of sand and sandy-pebble gravel, with a relative downward fining of grain size. We recorded in-situ gamma spectrometer measurements at each sample position and collected samples for inductively coupled plasma (ICP) analysis of radioactive elements to determine the radiation dose rate. All four IRSL samples were corrected for fading using a uniform 12% correction, which is the value used for previous studies in the Mojave Desert (Rhodes, 2015; Dolan et al., 2016).

The single-grain age plots reveal two distinct age populations within the two uppermost samples, with the older age populations yielding values of 5,560 ± 370 yb2020 (SRE14-01, 0.25 m depth) and 5,390 ± 410 years yb2020 (SRE14-02, 0.45 m depth), where IRSL ages are reported in years before 2020 when these samples were analyzed with 1-σ uncertainties (Table 1; Figure 4b). These older age populations are indistinguishable from the two lowermost samples (Figure 4b), which yielded ages of 5,640 ± 260 yb2020 (SRE14-03, 0.65 m depth) and 6,110 ± 370 yb2020 (SRE14-04, 0.95 m depth). We used the older age populations of the upper two samples (SRE14-01 and SRE14-02) with the third lowest sample (SRE14-03) to calculate an average age of deposition for the Qfc2 fan. We choose to not use the deepest sample (SRE14-04) and instead use the three youngest samples for our age estimate as these are more representative of

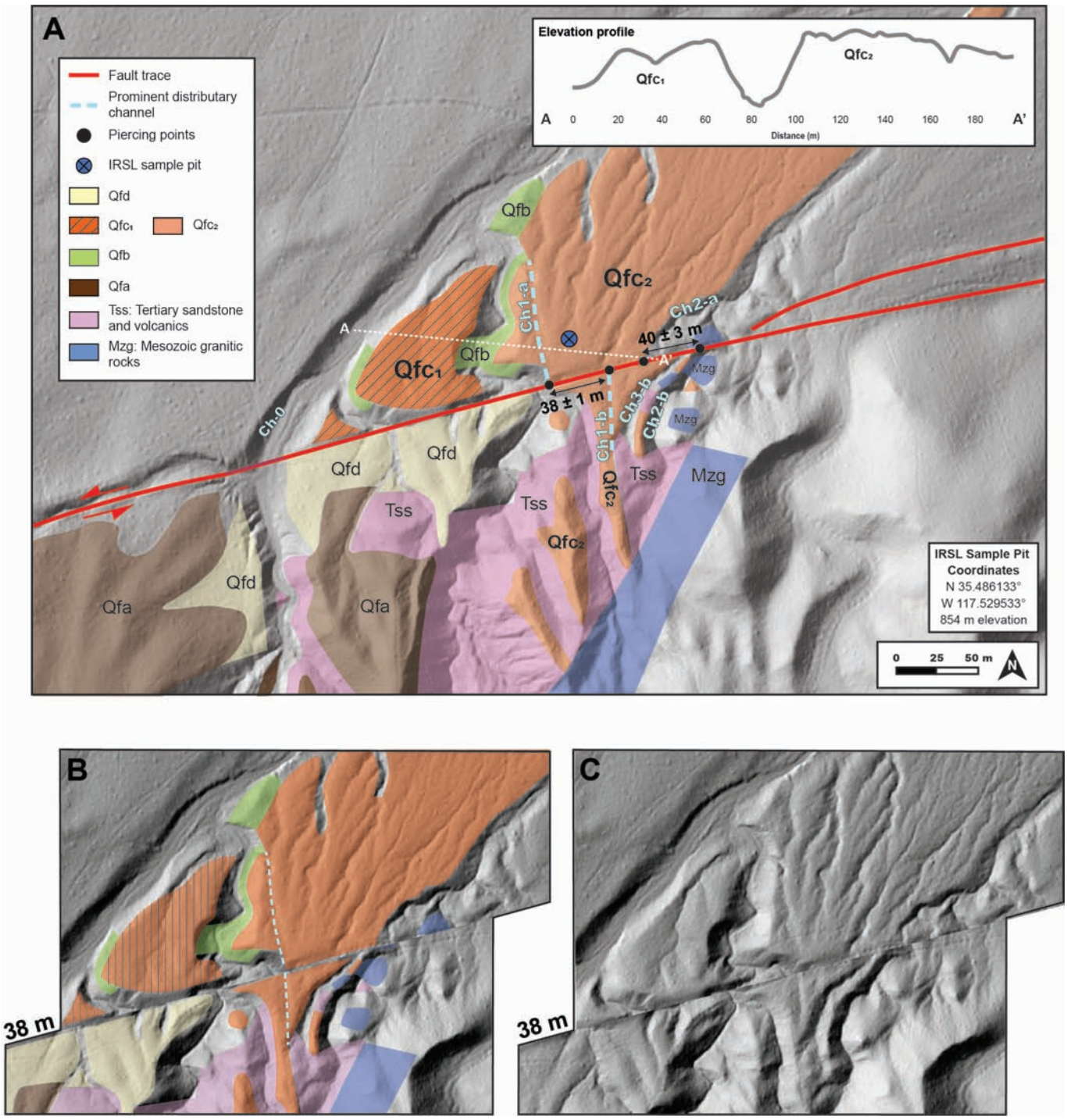

Figure 3 (a) Interpreted lidar-derived hillshade of the Summit Range East (SRE) site. Colors show various mapped alluvial fan surfaces (Qfa, Qfb, Qfc1, Qfc2, and Qfd) and other mapped rock units (Tss and Mzg). IRSL sample pit is shown by a blue circle and the fault trace is shown by red lines. Inset shows a topographic profile marked by a white dotted line (A-A') across Qfc1 and Qfc2 that suggests that the two fan segments may be the same fan. 38-m back-slipped restoration of the SRE site shown with (b) interpreted lidar-derived hillshade and (c) lidar-derived hillshade. The 38-m preferred offset measurement is based on the most plausible configuration of the channel (Ch-1) incised into the Qfc2 fan.

the geomorphic feature used to measure displacement.

We calculate a preferred estimate of the age of Qfc2 deposition by combining the three shallowest sample calendar dates with Gaussian errors using a chi-squared test using OxCal 4.4 (Reimer et al., 2020; Bronk Ramsey, 2009) yielding an age estimate of 5,570 ± 190 yb2020 (2-σ uncertainties) for the deposition of the Qfc2 fan (Figure 4c). Using the method to combine these dates described in Griffin et al. (2022) yields an indistinguishable age range of 5675 ± 356 yb2020. The younger age populations from samples SRE14-01 and SRE14-02 yielded ages of 1,890 ± 150 yb2020 and 1,820 ± 180 yb2020 (both report 1-σ uncertainties). See Supplementary Material 3.6 for a more detailed description of the interpretation of single-grain age distributions.

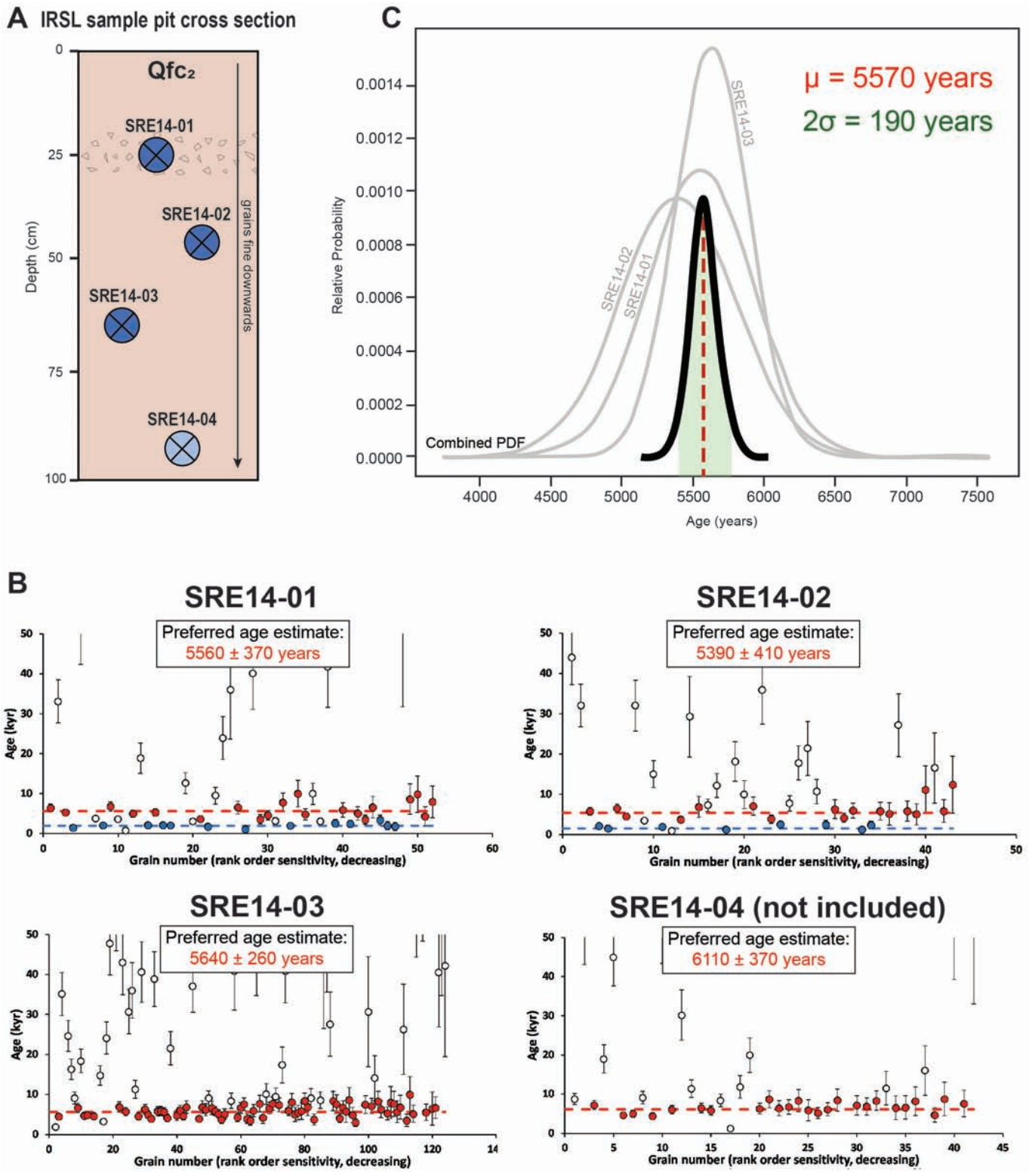

Figure 4 Age estimates for IRSL samples SRE14-01, SRE14-02, SRE14-03, and SRE14-04 that were collected from the Qfc2 fan at the Summit Range East site. (a) Cross-section diagram of Qfc2 sample pit showing depths at which samples were collected and general stratigraphy. Sample SRE14-04 is not included in the final slip rate calculation, (b) Single-grain potassium-feldspar post-IR infrared stimulated luminescence distribution data and preferred age estimates for each sample. (c) Preferred estimate of the age of Qfc2 deposition by combining three shallowest sample calendar dates with Gaussian errors using a chi-squared test using OxCal 4.4 (Reimer et al., 2020; Bronk Ramsey, 2009).

3.1.3 Slip Rate Calculation

We used our preferred offset value of 38 ± 1 m based on the prominent distributary channel (Ch-1) and the 5.57 ± 0.19 ka age as an estimate of Qfc2 fan deposition to determine a slip rate at the SRE site of 6.8 ± 0.3 mm/yr, with 2-σ uncertainties calculated in quadrature. Specifically, we constructed a triangular density function for the 38 ± 1 m offset of the Qfc2 and a Gaussian density function for the 5,680 ± 340 year age estimate of the Qfc2 fan

Site	Field code	Lab code	Stratigraphic unit	Depth (m)	Age (years)		1-σ
SRE	SRE14-01*	J0733	Qfc_2	0.25	1890	±	150
SRE	SRE14-01	J0733	Qfc_2	0.25	5560	±	370
SRE	SRE14-02*	J0734	Qfc_2	0.45	1820	±	180
SRE	SRE14-02	J0734	Qfc_2	0.45	5390	±	410
SRE	SRE14-03	J0735	Qfc_2	0.65	5640	±	260
SRE	SRE14-04	J0736	Qfc_2	0.95	6110	±	370
CW	GF16-01	J1385	Qfy	0.34	8490	±	490
CW	GF16-02	J1386	Qfy	0.52	8420	±	460
CW	GF16-03	J1387	Qfy	0.7	7100	±	560
CW	GF16-04	J1388	Qfy	1.05	12500	±	900
SRW	GF16-05	J1389	Qf2	0.41	7840	±	760
SRW	GF16-06	J1390	Qf2	0.63	9050	±	740
SRW	GF16-07	J1391	Qf2	0.84	6710	±	840

Table 1 Results of single-grain post-IR IRSL dating from Summit Range East (SRE), Summit Range West (SRW), and Clark Wash (CW). * denotes younger population within sample and is not used in calculation of average age of stratigraphic unit.

deposition. We then summed both distributions using pointwise addition to generate a joint probability density function (PDF) by combining offset and preferred age values and their uncertainties. Pointwise addition (i.e., statistical union) is used to combine PDFs because the samples were collected from the same unit, and we are interested in the probability that a date exists within any one of those ages. We also calculated a slip rate at this site using the full potential error range of 37-43 m and the 5.57 ± 0.19 ka age estimate of the Qfc2 fan, yielding a similar slip rate of 7.0 ± 0.7 mm/yr. The new ~6.8 mm/yr slip rate calculated using our tightly constrained offset for the SRE site is a minimum rate because an unknown amount of time may have elapsed between the cessation of fan deposition and the subsequent earthquake when offset of the Qfc2 fan began to accrue.

To determine the vertical component of slip of Qfc2, we measured the down-fan profile gradient north and south of the fault using lidar data to compare the elevation difference, yielding <0.5 m of vertical displacement over the same time period (ca. 5.6 ka) as the 38 ± 1 m offset. These measurements of left-lateral and vertical offset indicate that the Garlock fault at this site exhibits almost pure left-lateral slip with a ratio of ~76:1 (south-side up component of slip) shown in Figure S2.

3.2 Summit Range West

The Summit Range West (SRW) site was first identified by Clark (1973) and studied in detail by Ganev et al. (2012). Like the SRE site, the SRW site is located on the north-facing mountain front of the Summit Range on the central segment of the Garlock fault, 3 km west of the SRE site (Figure 2). At the SRW site, a large channel that drains much of the Summit Range flows northwards across the fault and has deeply incised into two alluvial fans, Qf1 and Qf2, both of which emanated from this same source drainage. The alluvial fan of interest (Qf2) was deposited atop the older and more laterally extensive Qf1 fan surface. The deeply incised channel has been sharply offset left-laterally by the Garlock fault.

3.2.1 Offset Measurements

Ganev et al. (2012) measured an offset at the SRW site of 70 ± 7 m based on the restoration of the incised edge of the Qf2 fan surface on the western margin of the channel. This western edge of the channel is present both upstream and downstream of the fault (Figure 5). The maximum offset estimate is based on a restoration of 77 m, because larger restorations shut off northward flow through the deeply-incised channel. The minimum offset estimate is based on restorations smaller than 63 m, resulting in a sharp, sedimentologically unlikely deflection of the Qf2 fan edge at the fault on the western side of the channel. Additionally, Ganev et al. (2012) measured an offset of 58 ± 4 m of the deeply incised thalweg of the channel and interpreted this somewhat smaller offset to have occurred after deeper incision of the channel, which they inferred might be related to major climate events at ~8-10 ka or 11.5 ka (younger than the age of initial incision of Qf2). This smaller ~58 m offset was interpreted to reflect gradual straightening of the channel during incision as the western channel wall south of the fault and the eastern channel wall north of the fault is more exposed to erosion during incision and downcutting. We follow Ganev et al. (2012) in using the 70 ± 7 m restoration of the incised edge of the Qf2 fan on the western margin of the channel in our slip rate calculation. We think this best reflects the location of the initial incision, which is the event that is constrained by the IRSL age data collected from Qf2.

3.2.2 Age Constraints

We collected three new post-IR IRSL samples from a 1.5-m-deep by 1-m-square pit (N 35.47834°, W 117.55943°, at an elevation of 1006 m) hand excavated into the Qf2 fan surface in steel tubes from sand-rich horizons in a vertical sequence at depths between 40-85 cm (Figure 6). We chose our sample pit location to be only a few meters from the pit from where Ganev et al. (2012) collected their 10Be depth profile to ensure we were dating the same surface. We recorded in-situ gamma spectrometer measurements at each sample position and collected

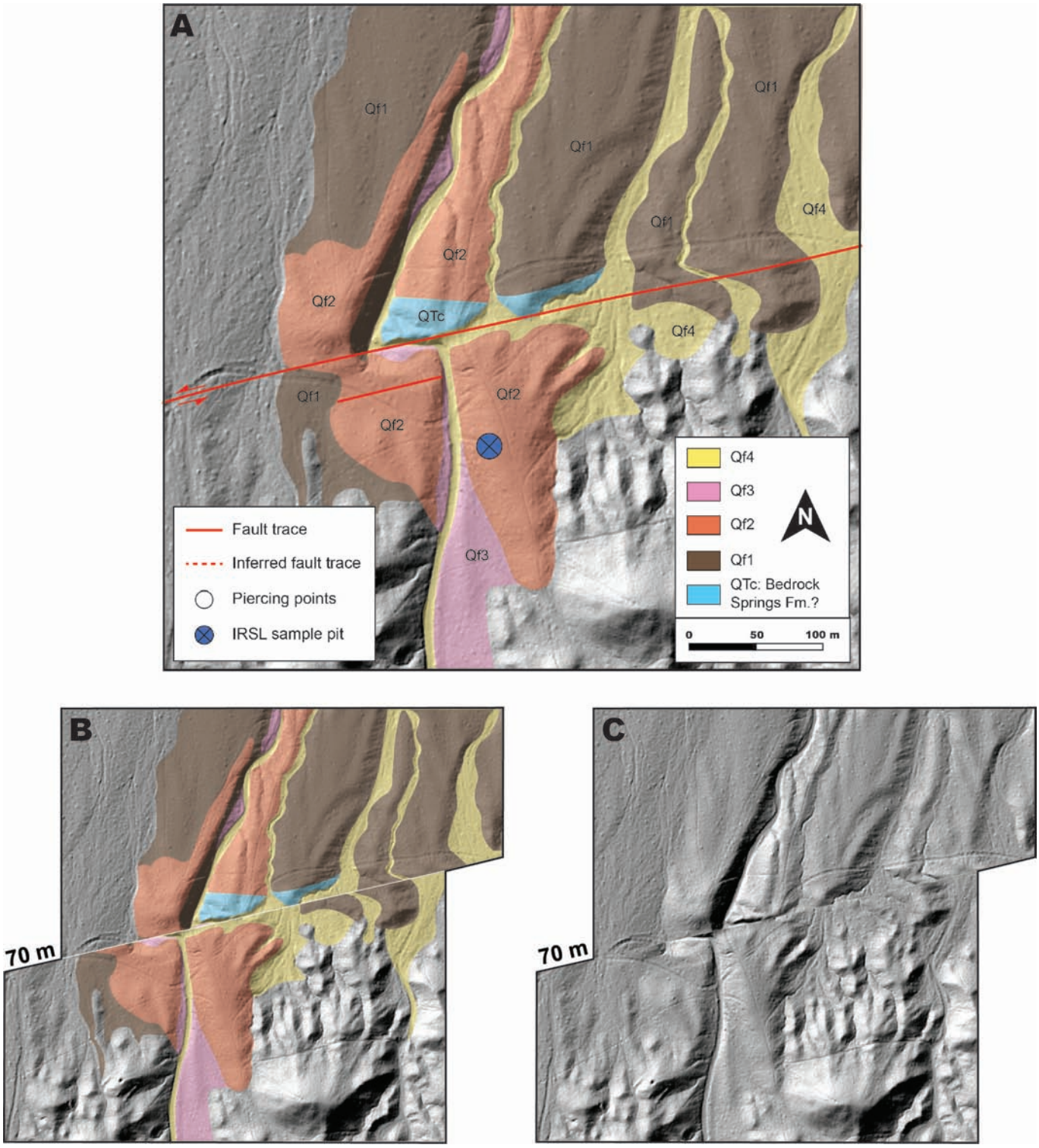

Figure 5 (a) Interpreted lidar-derived hillshade of the Summit Range West (SRW) site. Colors show various mapped alluvial fan surfaces (Qf1, Qf2, Qf3, and Qf4) and other mapped rock units (QTc). IRSL sample pit is shown by a blue circle and the fault trace is shown by red lines. 70-m back-slipped restoration of the SRW site shown with (b) interpreted lidar-derived hillshade and (c) lidar-derived hillshade. The 70-m preferred offset measurement is based on the restoration of the incised edge of the Qf2 fan surface on the western margin of the channel.

samples for Inductively Coupled Plasma (ICP) analysis.

The three IRSL samples, once corrected for fading using a uniform 12% fading correction (Rhodes, 2015; Dolan et al., 2016), yielded ages of 7840 ± 760 yb2020 (GF16-05, 0.41 m depth), 9050 ± 740 yb2020 (GF16-06, 0.63 m depth), and 6710 ± 840 yb2020 (GF16-07, 0.84 m depth), where IRSL ages are reported with 1-σ uncertainty in years before 2020 when these samples were analyzed (Table 1). We calculated an average age of Qf2 deposition by combining all three calendar dates with Gaussian errors using a chi-squared test using OxCal 4.4 (Reimer et al., 2020; Bronk Ramsey, 2009) yielding an age estimate of 7960 ± 900 yb2020 (2-σ uncertainties), which provides a maximum age for the initial incision

of the offset channel (Figure 6c). These new IRSL data demonstrate that earlier age estimates for the deposition of the Qf2 fan (Ganev et al., 2012) were too old. Specifically, Ganev et al. (2012) collected a Beryllium-10 (10Be) radionuclide depth profile from a pit located <5 m from the IRSL pit where samples GF16-05, GF16-06, and GF16-07 were collected, which yielded an age from the Qf2 fan surface of 13.3 +5.9/-1.0 ka. However, our new IRSL ages presented here demonstrate that the Qf2 fan was actually deposited at ca. 8 ka. This anomalously old 10Be age is consistent with the observations of Owen et al. (2011), who showed that there is significant 10Be terrestrial cosmogenic nuclide inheritance within cobbles and boulders in desert settings characterized by highly intermittent, short transport streams, suggesting that sediments are eroded and transported slowly in these regions, which can lead to overestimating the age of the dated feature.

3.2.3 Slip Rate Calculation

We used our preferred offset value of 70 ± 7 m and the 8.0 ± 0.9 ka age of the Qf2 fan to determine a slip rate at the SRW site of 8.8 ± 1.0 mm/yr, with errors calculated in quadrature and 2-σ uncertainty reported. Specifically, we constructed a triangular density function for the 70 ± 7 m offset of the Qf2 riser and a Gaussian density function for the 7960 ± 900-year age estimate of the Qf2 deposition. We then summed both distributions to generate a joint PDF to combine offset and preferred age and their uncertainties. This new ~8.8 mm/yr slip rate for the SRW site is a minimum rate because an unknown amount of time may have elapsed between the cessation of fan deposition and the occurrence of the next earthquake (i.e., when offset of the Qf2 fan began to accrue).

3.3 Clark Wash

The Clark Wash (CW) site was first identified by Clark (1973) and studied in detail by McGill et al. (2009). The CW site is located near the eastern end of the western segment of the Garlock fault, south of the southwesternmost Sierra Nevada (Figure 7).

The CW site comprises an alluvial fan complex sourced from an ~1 km2 area of granitic bedrock (Smith, 1964) of the southern Sierra Nevada batholith via Clark Canyon. At the CW site, a latest Pleistocene alluvial fan (Qfo) was deposited containing charcoal that yielded calibrated radiocarbon ages ranging from 22.7 to 13.3 ka (Figure 8a). The Qfo fan is composed of alternating layers of grain-supported, small-pebbly-to-coarse-sand stream deposits and matrix-supported debris flows (McGill et al., 2009). Several trenches exposed Qfo capped by a buried soil which, in turn, was buried by a ~1-m thick veneer of younger (latest Pleistocene to early Holocene) alluvial deposits (Qfy), which have not been directly dated in previous studies. Following the deposition of Qfo, development of buried soil, and deposition of Qfy, Clark Wash incised deeply into these fan deposits (Figure 8a) and partially filled with fluvial-sourced, thickly bedded, gravelly sand (Hoa) and interfingering sandy colluvium derived from the channel wall and from the Garlock fault scarp (Hoc; McGill et al., 2009). Hoa and Hoc deposits were only exposed in trenches and are located beneath stream deposits (Hya) and Holocene colluvium (Hyc) shown in Figure 6a. Calibrated radiocarbon dates from detrital charcoal and hearth features within these deposits range from 8.0 – 6.8 ka. A younger episode of channel incision and fill occurred during late-Holocene time, as shown by Hya deposits exposed in one of the McGill et al. (2009) trenches south of the fault containing a ca. 2.5 ka charcoal sample (McGill et al., 2009), which, when recalibrated in this study using Oxcal version 4.4 and the most up-to-date calibration curve (IntCal20, Bronk Ramsey, 2009; Reimer et al., 2020) yielded an age of 2530 ± 220 cal. yrs B.P. (2-σ uncertainty).

3.3.1 Offset Measurements

The refined early Holocene slip rate measurement presented here is based on the offset of Clark Wash incised into the Qfy fan. Specifically, a 2-to-3-m-tall terrace riser separating Qfy from younger Hyc and Hya (Figure 8a). This well-defined offset is based primarily on the restoration of the northeastern channel wall. The offset value for this feature was measured as 66 ± 6 m by McGill et al. (2009) using a combination of surveyed piercing points along the top of the terrace riser on the northeastern edge of Clark Wash, the inner edge of the younger, Clark Wash fluvial strata (Hoa) exposed in trenches where it had been buried by colluvium (Hoc and Hya), and a photogrammetric map with 0.5 m contours.

Reevaluation of this offset in this study using lidar-derived hillshade confirms that the northeastern terrace riser is left-laterally offset by 66 ± 6 m (Figure 8b and c). The offset of the southwestern terrace riser cannot be constrained as tightly because the piercing point where the southwestern wall of the channel that once intersected the southeastern side of the fault has been eroded by Clark Wash. Using a photogrammetric map with 0.5 m contours, McGill et al. (2009) estimated the offset to be 65 ± 7 m, consistent with (but with broader uncertainty than) the offset measured for the northeastern wall. Figure 8a shows one likely projection of piercing points for the southwestern wall of the channel, which results in an offset estimate of 60 m.

3.3.2 Age Constraints

Radiocarbon ages presented here were originally collected and calibrated by McGill et al. (2009) and were recalibrated in this study using Oxcal version 4.4 (Reimer et al., 2020; Bronk Ramsey, 2009). We combined these ages with new IRSL data collected from a pit excavated into the Qfy fan, which was not dated by McGill et al. (2009), because no charcoal samples were found from it. Because Qya is the youngest deposit that has been incised by the offset channel, its age is critical to providing the tightest possible maximum age constraint on the slip rate at this site. In this study, the minimum age estimates for the onset of offset of the channel wall separating Qfy (and the underlying Qfo) from Hoa was determined from recalibrated radiocarbon dates from the same charcoal samples from Hoa used in McGill et al.

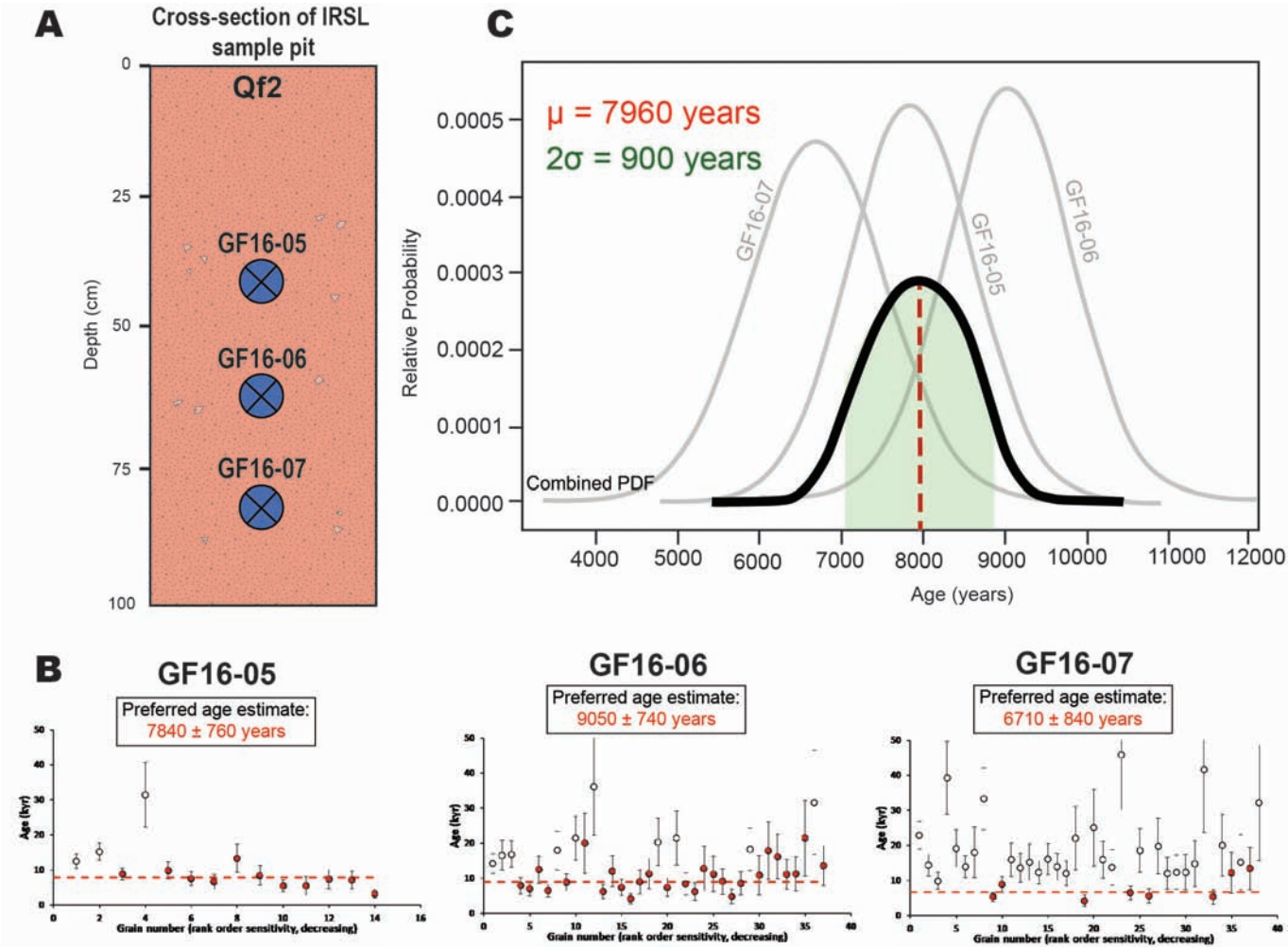

Figure 6 Age estimates for IRSL samples GF16-05, GF16-06, and GF16-07, which were collected from the Qf2 fan at the Summit Range West site. (a) Cross-section view of Qf2 sample pit showing depths at which samples were collected. (b) Single-grain K-feldspar IRSL distribution data and preferred age estimates for each sample. (c) Preferred estimate of the age of Qf2 deposition by combining all three calendar dates with Gaussian errors using a chi-squared test using OxCal 4.4 (Reimer et al., 2020; Bronk Ramsey, 2009).

(2009) slip rate estimate. However, whereas McGill et al.'s maximum age estimate for the incision of this riser was based on the youngest age from Qfo (13.3 ka), in this study a much tighter maximum age estimate was determined from our new IRSL data collected from the previously undated Qfy fan deposits.

Maximum age using post-IR infrared stimulated luminescence dating We collected four IRSL samples in steel tubes from sand-rich horizons from a pit (N 35.20578°, W 118.08663° at an elevation of 864 m) excavated into the Qf2 surface in a vertical sequence at depths between 35-104 cm (Figure 9a). We recorded in-situ gamma spectrometer measurements at each sample position and collected samples for ICP analysis. Post-IR IRSL luminescence ages from these samples reveal a layered fan structure. The three upper samples (GF16-01, GF16-02, and GF16-03) collected at depths between 34-70 cm were from Qfy. After correcting for fading using a uniform 12% correction, these samples yielded ages of 8490 ± 490 yb2020 (GF16-01; 0.34 m depth), 8420 ± 460 yb2020 (GF16-02; 0.52 m depth), and 7100 ± 560 yb2020 (GF16-03; 0.70 m depth), where IRSL ages are reported with 1-σ uncertainties reported in years before 2020 (Table 1). We calculate the age of Qfy fan deposition by combining the three upper samples with Gaussian probability distribution using a chi-squared test (based on OxCal4.4; Reimer et al., 2020; Bronk Ramsey, 2009). This yields a preferred age of Qfy deposition of 8095 ± 575 years (2-σ uncertainty; Figure 9c).

We collected sample GF16-04 at 105 cm depth from the same pit as the three uppermost samples. This sample, which yielded an age of 12500 ± 900 yb2020 after a uniform 12% fading correction (1-σ uncertainty), was collected from Qfo deposits that underlie the Qfy deposits at this site. The Qfo fan deposits were readily distinguished from Qfy deposits because they are very well consolidated with a reddish matrix of translocated clay, whereas the overlying Qfy fan deposits are poorly sorted, massive, and matrix supported. The depth of the contact between Qfy and Qfo was similar to that observed in McGill et al. (2009) trenches. Since we are concerned with the 66 ± 6 m offset of the Qfy fan, we do not use the ~12.5 ka age of GF16-04 in our slip rate calculations, but we note that it is consistent with the youngest

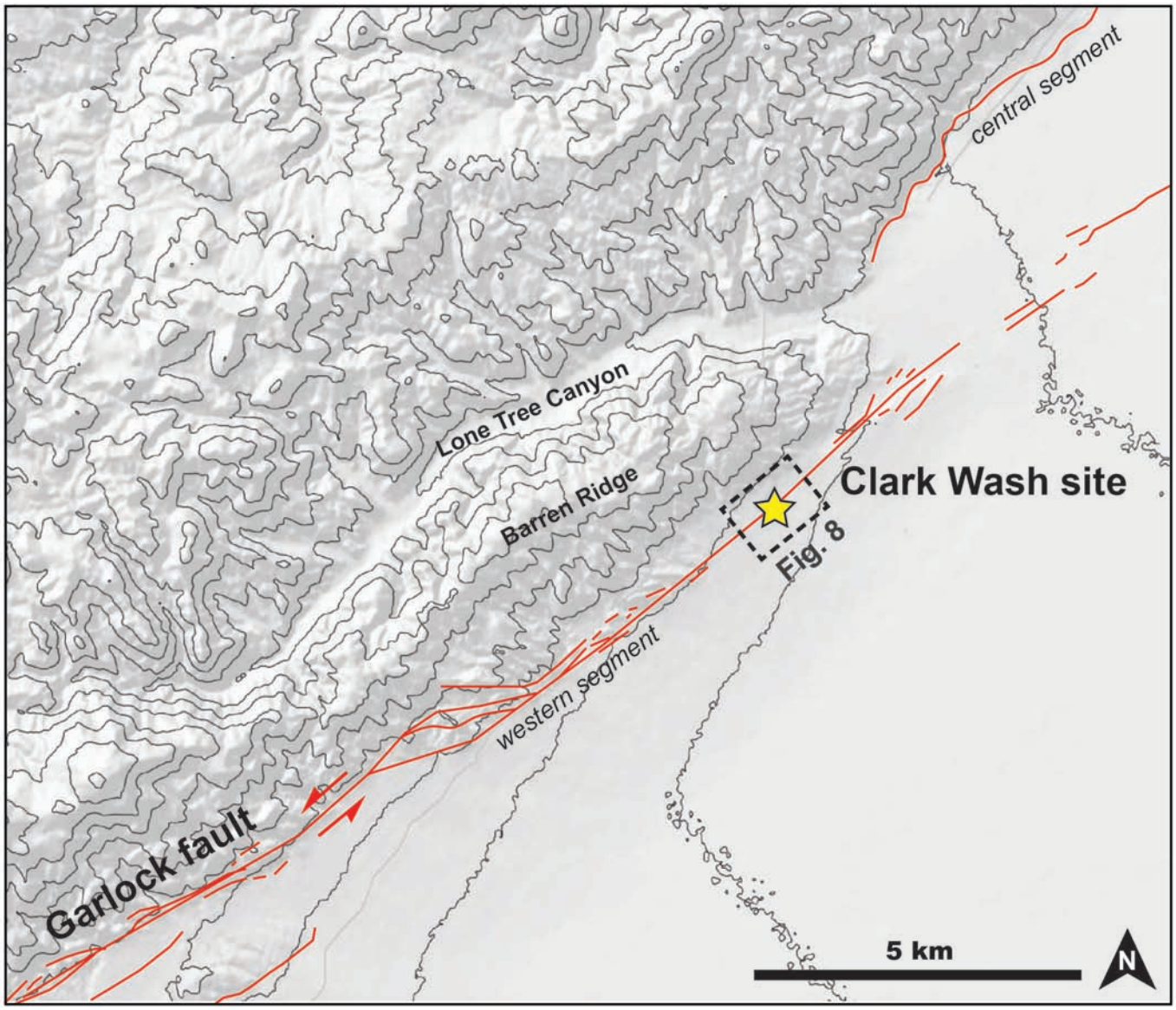

Figure 7 Regional topographic map of the Clark Wash site with a contour interval of 100 m. The Clark Wash site is located at the northeastern extent of the western Garlock fault segment adjacent to the 2-3 km wide step over at Koehn Lake at N 35.214608° W 118.075739°. The black dashed box outlines the location of Figure 8a.

radiocarbon age from Qfo (13.3 ka) that was reported by McGill et al. (2009).

Minimum age using radiocarbon dating McGill et al. (2009) collected eight charcoal samples from the deepest part of a trench excavated into the Holocene channel fill of Clark Wash (Hoa) and colluvium (Hoc) sourced from the channel wall of the incised Qfo fan and its overlying veneer of Qfy. We recalibrated radiocarbon dates for these eight charcoal samples using OxCal version 4.4 (Reimer et al., 2020; Bronk Ramsey, 2009). The oldest ages from Hoa and Hoc provide a minimum bound on the age of initial incision of the Qfy fan by Clark Wash, because Hoa and Hoc were deposited after the incision that formed the channel wall that is now offset by 66 ± 6 m. We derived minimum age constraints for this incision in two ways: (A) the average age derived from all eight radiocarbon samples from the Hoa channel-fill deposits and the Hoc colluvial deposits that interfinger with Hoa, and (B) the calibrated age of the stratigraphically lowest and oldest sample (H14-6N-44).

We combined the eight radiocarbon ages using Gaussian probability distributions using a chi-squared test (based on OxCal4.4; Reimer et al., 2020; Bronk Ramsey, 2009), yielding an average age of the channel-fill deposits of 7,870 ± 88 cal. yrs BP (95% confidence interval; Figure 9d). A similar, but slightly older, maximum age for channel incision of 8,065 ± 135 cal. yrs B.P was determined using the calibrated age of the oldest charcoal sample, H14-6N-44, collected from the lowest stratigraphic level of the trench (McGill et al., 2009).

Average age for fault offset The age of the onset of fault offset for the channel wall that separates Qfo and its overlying cap of Qfy from Hoa is between the age of deposition of Qfy (8095 ± 575 years ago), which is older than the initial incision of the channel, and the age of the oldest deposits within the channel, Hoa/Hoc (7,870 ± 88 cal. yrs BP), which is younger than age of initial channel incision. To calculate the time interval between the

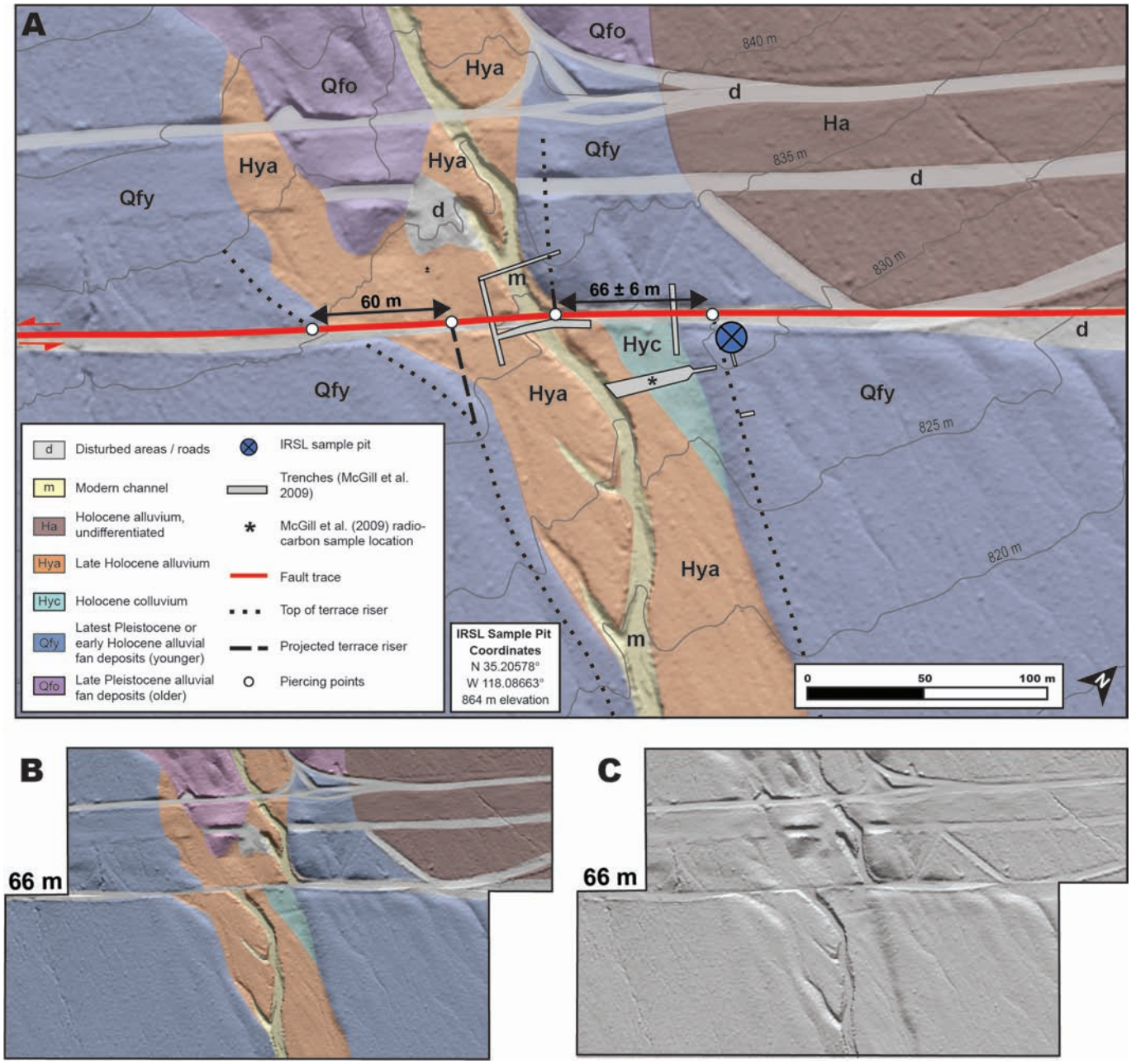

Figure 8 (a) Interpreted lidar-derived hillshade of the Clark Wash (CW) site. Colors overlying lidar-derived hillshade show various mapped surfaces (disturbed surface, modern channel, various aged alluvium, and colluvium). IRSL sample pit is shown by a blue circle and the fault trace is shown by a red line. Eight of the ten trenches that were excavated by McGill et al. (2009) fall within the area shown in this figure and are marked by gray boxes. The location beneath which radiocarbon samples from Hoa were collected is indicated by the asterisk within one of the trenches. The 66-m back-slipped restoration of the CW site is shown with (b) interpreted lidar-derived hillshade and (c) lidar-derived hillshade. The 66-m preferred offset measurement is based on the restoration of the northeastern channel wall (see Figure S1 for minimum and maximum restorations).

minimum and maximum age, we used the RISeR program (Zinke et al., 2017, 2019) to calculate the probability function representing the interval between the age PDFs derived from the upper terrace (determined from IRSL) and the lower terrace (determined from radiocarbon). This yielded an age constraint for the age of incision of 8010 +1115/-210 years (95% confidence interval, Figure 9e).

3.3.3 Slip Rate Calculation

To calculate a revised slip rate for the Clark Wash site, we combine the estimate for the age of incision of the offset channel wall (8010 +1115/-210 years) with the preferred restoration of the offset channel wall of 66 ± 6 m, yielding a slip rate of 8.2 +1.4/-0.8 mm/yr (2-σ uncertainty calculated in quadrature). This rate is based on the well-constrained age of incision into the Qfy fan surface and subsequent deposition into Clark Wash, and does not consider the possibility or the unknown duration of time between this incision event and the first

Field code	Lab code	Uncalibrated age (years B.P.)	Mean (cal. years B.P.)		2-σ uncertainty	Stratigraphic unit
H14-6N-56	AA-14555	6812 ± 91	7667	±	86	Hoa
H14-6N-17	AA-14551	6888 ± 88	7737	±	87	Hoc
H14-6N-133	AA-14552	6918 ± 71	7760	±	75	Hoc
H14-6N-50B	AA-14553	6968 ± 109	7802	±	100	Hoc
H14-6S-31	AA-14549	7040 ± 94	7857	±	91	Hoc
H14-6S-1	AA-14550	7056 ± 103	7872	±	101	Hoc
H14-6N-140/141/142	Beta-74108	7170 ± 140	7997	±	146	Hoc
H14-6N-44	AA-16339	7240 ± 59	8066	±	68	Hoa

Table 2 Results of radiocarbon dating from the Clark Wash site. Calibrations based on IntCal20 calibration curve using OxCal 4.4 (Reimer et al., 2020; Bronk Ramsey, 2009)

earthquake to occur after the incision. Therefore, this rate should be considered a minimum slip rate.

4 Discussion

4.1 Multi-Millennial Slip Rate Variations

The three new slip rates presented here from the Summit Range East (SRE), Summit Range West (SRW), and Clark Wash (CW) sites add to the growing incremental slip rate record for the western and central Garlock fault (McGill and Sieh, 1993; McGill et al., 2009; Ganev et al., 2012; Rittase et al., 2014; Dolan et al., 2016). Advanced luminescence dating techniques have allowed us to precisely date the deposition of alluvial fans at the SRW site to revise and more tightly constrain the previous, slower slip rate estimate of 5.3 +1.0/−2.5 mm/yr averaged over 13.3 ka documented by Ganev et al. (2012), to a revised rate of 8.8 ± 1.0 mm/yr averaged over 8.0 ka. In addition, these new age data have allowed us to date a previously undated unit at the Clark Wash site, resulting in a substantially tighter bound on the slip rate at that site of 8.2 +1.0/-0.8 mm/yr averaged over the past 8.0 ka, compared to the previously published rate of 7.6 +3.1/-2.3 mm/yr averaged over a time interval spanning 0 to 9.3 ka (McGill et al., 2009). Finally, we also have documented a new slip rate of 6.8 ± 0.3 mm/yr over the past 5.6 ka at a new site–SRE.

Combining the three new and refined slip rates with (a) previously published records of incremental slip rate averaged over different time periods during Holocene to latest-Pleistocene time, and (b) the most recent earthquake (MRE) age documented at the El Paso Peaks (EPP) site (Dawson et al., 2003) and the Christmas Canyon site (Pena, 2019), allow us to construct a detailed time-displacement history for the central Garlock fault since ca. 8 ka (Figure 10). This record facilitates testing for possible correlations between periods of earthquake clustering and seismic lulls with potential accelerations and decelerations of fault slip rate spanning multiple earthquake cycles, as has been suggested in previous studies (e.g., Dawson et al., 2003; Dolan et al., 2007, 2016; Ganev et al., 2012; Rittase et al., 2014).

The incremental slip history of the central Garlock fault is marked by significant (factor of 2 to 5 times) variations in slip rate spanning cycles of thousands of years (~2 to 4 ky) during latest Pleistocene and Holocene time. Specifically, the new slip rate averaged since 5.7 ka of 6.8 ± 0.3 mm/yr from the central segment of the fault (SRE site) is consistent with previous studies of longer-term average slip rates since latest-Pleistocene to early-Holocene time of 5 to 8 mm/yr (Clark and Lajoie, 1974; McGill and Sieh, 1993; Ganev et al., 2012; McGill et al., 2009). However, our revised ca. 8 ka-averaged slip rates of 8.8 ± 1.0 mm/yr from the central segment (SRW site) and 8.2 +1.4/-0.8 mm/yr from the eastern extent of the western segment (CW site), reveal two of the fastest long-term (>6 ka) slip rates of any site documented along the Garlock fault.

Incremental slip rates for the central Garlock fault for various time intervals since the latest Pleistocene vary from 3.1 mm/yr to 13.6 mm/yr (Figure 10b). We calculated incremental slip rates between age-displacement pairs using RISeR's analytical formulation (Zinke et al., 2017, 2019) based on Bayesian statistics, which resamples the age and displacement measurements according to their PDFs to calculate a slip rate over a specified time interval. We chose an analytical sampling approach (rather than Markov Chain Monte Carlo sampling) as it is ideal for data sets in which dated markers are independent (i.e., do not overlap within uncertainty), which is the case for the data presented here (see Supplementary Material 4.1). Differences in slip rate between the SRW and SRE sites are due to the different time periods that they sample, not due to changes in slip rate along strike, because these two sites are separated by only a few kilometers along a continuous, structurally simple section of the fault. The CCW slip rate also lies along this same simple section of the fault, so we infer that all three incremental slips reflect the same changes of rate along the central Garlock fault.

Periods of faster slip on the central Garlock fault (e.g., 0.5-1.9 ka and ca. 5-8 ka) appear to correspond with bursts of earthquake recurrence recorded on the central segment, and slower periods appear to correspond with periods of relative seismic quiescence. For instance, the paleoseismic record generated by Dawson et al. (2003) at the EPP site, 20 km west of the SRE site on the central segment (Figure 1), displays a four-earthquake cluster between 0.5 and 2.0 ka, corresponding to a faster-than-average slip rate during this period of >14.0 +2.2/-1.8 mm/yr (Dolan et al., 2016). Previously, the absence of any detectable paleo-surface ruptures between 1.9 ka and 5.1 ka in the EPP trench suggested that the Garlock fault did not generate any surface-

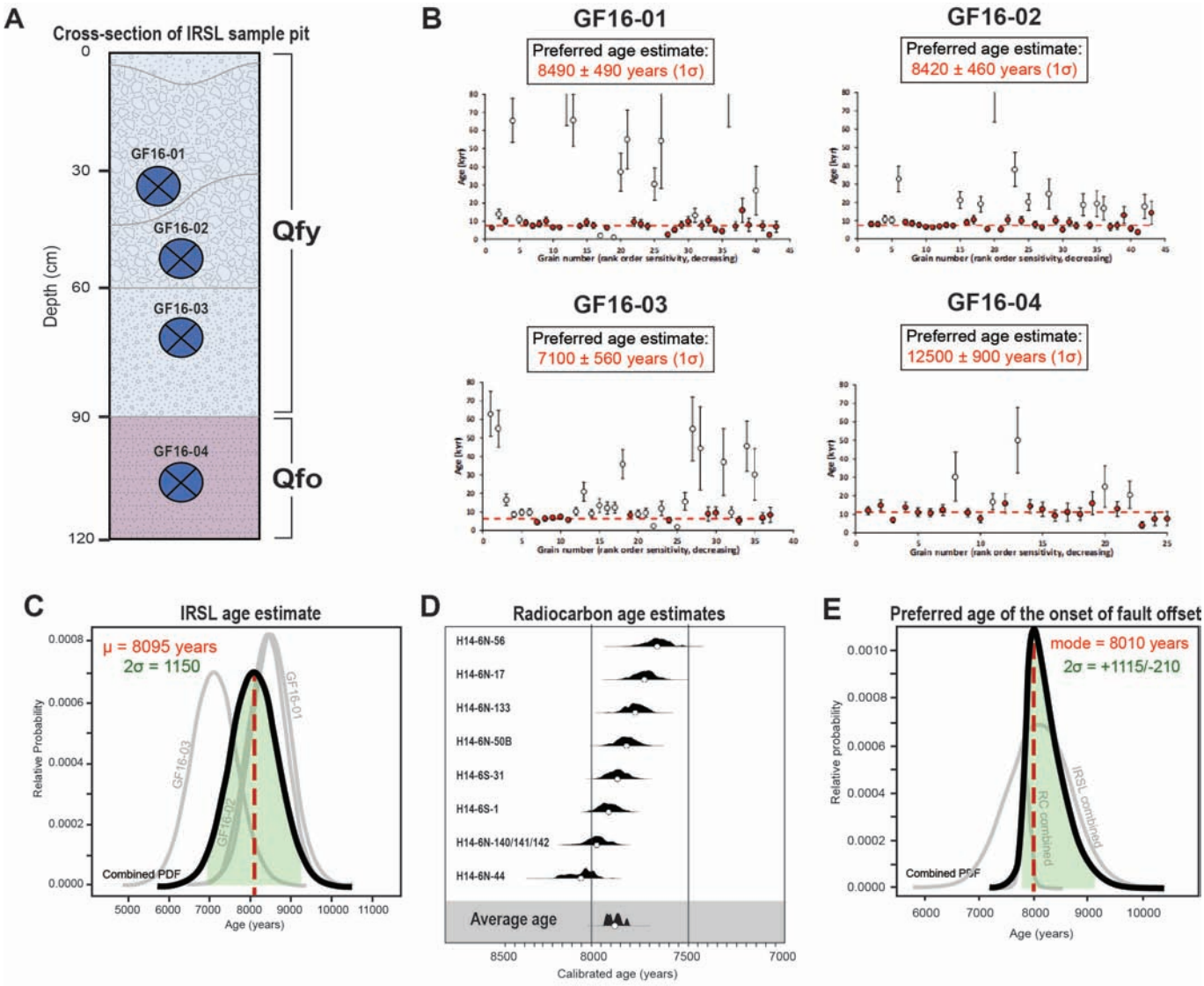

Figure 9 Age estimates for IRSL samples GF16-01, GF16-02, GF16-03, and GF16-04 collected at the Clark Wash site. (a) Cross-section view of IRSL sample pit showing depths that samples were collected. GF16-01, GF16-02, and GF16-03 were collected from Qfy, whereas GF16-04 was collected from Qfo. (b) Single-grain K-feldspar post-IR IRSL distribution data and preferred age estimates for each sample. (c) Preferred estimate of the age of Qfy deposition by combining all four IRSL dates with Gaussian errors using a chi-squared test using OxCal 4.4 (Reimer et al., 2020; Bronk Ramsey, 2009). (d) Probability density functions for the eight radiocarbon charcoal samples ages collected from the Clark Wash site calculated using OxCal version 4.4 (Reimer et al., 2020; Bronk Ramsey, 2009). Average age of all eight samples was calculated using the OxCal combine function. (e) Age estimate of initial onset of fault offset calculated by finding the PDF representing the interval between (c) and (d).

rupturing earthquakes for more than 3,000 years (Dawson et al., 2003), which Dolan et al. (2016) interpreted to have resulted in a "zero" slip rate over this time interval. However, given that 38 ± 1 m of left-lateral slip has occurred at the SRE site since ~5.6 ka, and 26 +3.5/-2.5 m of slip has occurred at the CCW site since ~1.9 ka, it is clear that 12 +1/-2.5 m of slip occurred during the ~3.7 ky interval between 1.9 ka and 5.6 ka. This results in an incremental slip rate of 3.1 ± 0.4 mm/yr during this period of relative quiescence. Additionally, Dawson et al. (2003) recorded one paleo-surface rupture at ~5.1 ka within this slow-slip interval between 1.9-5.6 ka (Figure 10). However, as noted above, we suspect there may have been one or more additional paleoearthquakes during this slow-slip interval that were not recognized at the EPP trench. Preceding the 1.9-5.6 ka slow-slip interval, we use RISeR (Zinke et al., 2017, 2019) to calculate an incremental slip rate of 12.9 +3.2/-2.3 mm/yr between 5.7 ka and 8.0 ka. Although we do not have incremental slip rate data for the western Garlock fault, it is noteworthy that the average 8.0 ka slip rate at the CW site, on the western Garlock fault, is very similar to the average slip rate for the past 8.0 ka on the central Garlock fault at the SRW site.

These new results add to the growing body of evidence suggesting that the Garlock fault experiences a highly irregular temporal pattern of incremental slip (i.e., non-constant behavior) over periods that span multiple earthquake cycles. Namely, the incremental slip history of the central Garlock fault can be characterized as a period of relatively fast strain release during the late Holocene (0.5-1.9 ka), preceded by a pe-

riod of slow but not zero strain release during the mid-Holocene (1.9-5.0 ka), which in turn was preceded by another period of fast strain release during the mid-to-late-Holocene (ca. 5-8 ka). The new slip rate data presented here offer a more robust and nuanced view of the slip history of the Garlock fault since the latest Pleistocene.

4.2 Comparison of Geodetic Slip-Deficit Rate with Incremental Geologic Slip Rates

Supporting the observations of variations in elastic strain release rate through time suggested by our new incremental slip rate variations from sites along the western and central Garlock fault, the fast (8.2-8.8 mm/yr) average geologic slip rates since early Holocene time, averaged over 65-70 m of slip and numerous earthquakes, do not match decadal-scale geodetic slip-deficit rates in the region. Specifically, geodetic slip-deficit rates measured along the Garlock fault suggest negligible, to slow, left-lateral strain accumulation (~0-3 mm/yr) over the past several decades (Savage et al., 1981, 1990, 2001; Gan et al., 2000; McClusky et al., 2001; Miller et al., 2001; Peltzer et al., 2001; Meade and Hager, 2005; Evans et al., 2016). A recent block model suggests a slip-deficit rate for the central Garlock fault of ~2.6 ± 3.0 mm/yr (Evans, 2017b). These observations are inconsistent with the geologic slip rates averaged since early Holocene time that we document for the western and central Garlock fault (this study) and more closely resemble the ~3 mm/yr slip rate averaged over the relative seismic lull between ca. 2 ka and 5 ka (Figure 10a). This geologic-geodetic rate discrepancy is consistent with the possibility that relatively slow rates of interseismic fault loading for the Garlock fault could correlate with periods of relatively slow fault slip, as has been suggested for other faults (e.g., Gauriau and Dolan, 2024), which may be correlated with the current quiet period in seismic slip and earthquake occurrence since the MRE ca. 500 years ago (Dawson et al., 2003). Moreover, geodetically constrained models of elastic strain accumulation along the Mojave section of the San Andreas fault estimate a long-term slip rate of ~28 mm/yr (Moulin and Cowgill, 2023), which suggest similar temporal slip variations as the Garlock fault, with decadal-scale geodetic slip-deficit rates of 15 ± 3 mm/yr (Evans, 2017b), only about half as fast as the long-term geologic slip rate of 35 mm/yr (Evans, 2017b) for the Mojave section of the San Andreas fault. Hearn et al. (2013) and Hearn (2022) suggest that the geodetic slip-deficit and geologic slip rate discrepancy on the Mojave section of the San Andreas fault can be partially explained by a "ghost transient" associated with the 1857 M~7.8 Fort Tejon earthquake, where the relatively slow elastic strain deformation on the Mojave section of the San Andreas fault could be partially caused by long-term viscoelastic relaxation of the lithospheric mantle and lower crust following past earthquakes (e.g., 1857 Fort Tejon). Interestingly, the GPS velocity perturbations caused by large earthquakes on the Garlock Fault (i.e., MRE) do not influence block-model geodetic slip-deficit rates, which suggests that the discrepancy between geodetic slip-deficit and geologic slip rates for the Garlock Fault is not due to a ghost transient. If this apparent geodetic-geologic discrepancy for the Garlock fault is accurate (and some have suggested that it is not; e.g., Chuang and Johnson, 2011; Platt and Becker, 2013) (but see Evans, 2017a), it supports the notion that this region is experiencing temporal variations in both strain accumulation and release spanning millennia and several tens of meters of fault slip.

4.3 Evaluation of Driving Mechanisms for Garlock Fault Slip

The similar Garlock fault slip rates of 8.2 and 8.8 mm/yr averaged over the past ca. 8.0 ky that we document at the CW and SRW sites indicate that, on average, the eastern part of the western segment and the western part of the central segment have slipped at approximately the same average rate over the past 8 ky (Figure 10a). Although additional incremental slip rate measurements from the western segment of the Garlock fault are needed to determine whether these two fault sections experienced similar slip histories throughout Holocene time, the newly revised Clark Wash slip rate from the western segment, together with detailed Holocene slip history for the central Garlock fault (Figure 10), allows us to evaluate models of potential driving forces for slip on the central Garlock fault (e.g., Hatem and Dolan, 2018). For example, the SRW and SRE sites are located on a part of the Garlock fault embedded within the westernmost part of the ECSZ region of N-S dextral shear, where the fault may be partially loaded by clockwise rotation (Guest et al., 2003; McGill et al., 2009; Hatem and Dolan, 2018; Garfunkel, 1974). In contrast, the CW site is located west of the western edge of this zone of dextral shear, and therefore this segment of the fault is not being loaded via rotation within the ECSZ dextral strain field. Thus, the similarity of the ca. 8 ka rates at SRW and CW indicates that very little (and potentially almost none) of the slip on the central segment of the Garlock fault is a result of rotation-induced loading on these timescales. Rather, these new rates support the model proposed by Hatem and Dolan (2018), where the western and central segments of the Garlock fault are loaded primarily by lateral extrusion associated with N-S shortening in the region of the more westerly-striking section of the San Andreas fault bordering the Mojave Desert. This model suggests that the western and central segments of the Garlock fault will accommodate strain at an increased rate during periods when the San Andreas fault is slipping faster (e.g., Dolan et al., 2007). Moreover, these new slip rates from both the western and central Garlock fault provide a detailed record that can be compared with similar records from the San Andreas fault and ECSZ which have yet to be documented.

4.4 Implications for Probabilistic Seismic Hazard Assessment

Most physics- and statistics-based seismic hazard models typically follow the assumption that faults are loaded at a constant rate (i.e., strain accumulation and release rates remain constant between earthquake cycles

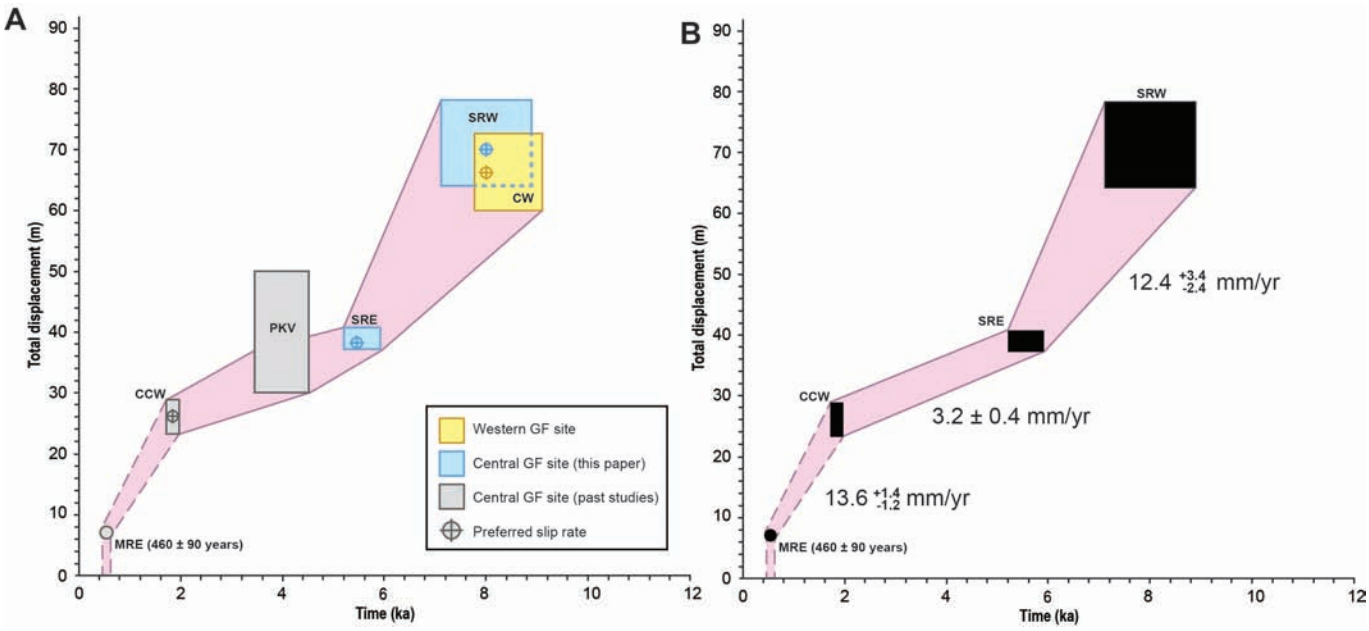

Figure 10 (a) Incremental slip history for the central and western Garlock fault including sites: CCW - Christmas Canyon West slip rate site (Dolan et al., 2016), CW - Clark Wash (this paper, building on McGill et al., 2009), MRE - most recent earthquake recorded by Dawson et al. (2003), SR - Slate Range slip rate site (Rittase et al., 2014), SRE - Summit Range East slip rate site (this paper), SRW - Summit Range West slip rate site (this paper, building on Ganev et al., 2012). (b) Incremental slip rates for the central Garlock fault calculated using RISeR (Zinke et al., 2017, 2019) using only the most tightly constrained rates from a 16-km-long section of the central part of the fault.

except for brief periods of post-seismic deformation). However, many studies, including this one, challenge this assumption, and suggest that it may not be appropriate since at least some faults have been shown to experience periods of faster-than-average slip separated by periods of slower-than-average slip (e.g., Weldon et al., 2004; Dolan et al., 2007; Ninis et al., 2013; Onderdonk et al., 2015; Dolan et al., 2016; Zinke et al., 2017, 2019, 2021; Hatem et al., 2020). As an example, it is evident from the updated incremental slip rate record shown in Figure 10 that the central (and possibly western) Garlock fault experiences temporally variable slip rates, during which fault slip has sped up and slowed down over millennial time scales, with fast periods spanning multiple earthquakes and 25-30 m of displacement. These results support the idea that non-constant behavior may be the expected mode of slip through time on faults such as the Garlock fault that lie within structurally complex fault networks, as suggested by Gauriau and Dolan (2021), who have shown that non-constant fault slip through time may be a response to complex stress interactions within structurally complicated fault systems involving either temporal variations in fault strength and/or kinematic interactions between faults within a plate boundary system. If rates of elastic strain accumulation also vary through time, as suggested by the geodetic-to-geologic rate discrepancy for the Garlock fault, then PSHA models based on the assumption of constant strain accumulation and release may not provide a useful prediction of near-future fault behavior. Gauriau and Dolan (2024) have shown that such geologic-to-geodetic discrepancies may be typical for faults such as the Garlock fault that lie within complex plate boundary fault systems.

Such results are of fundamental importance for probabilistic seismic hazard assessment, which relies on fault slip rates as a basic input parameter. But if fault slip rates on many faults vary through time, as in the case of the Garlock fault documented in this paper, it remains unclear what the "correct" slip rate is for use in PSHA. As detailed by Van Van Dissen et al. (2020), there are multiple ways of dealing with this under-constrained aspect of hazard estimation, including assuming very large bounds on the potential variability in earthquake recurrence that encompass the entire range of slip rate variability revealed by detailed incremental fault slip-rate records like the one detailed herein. But treating the variability of future earthquake recurrence in this manner yields little predictive value, given the large error ranges that result from this approach. If, alternately, we use a single slip rate calculated over some arbitrary displacement range, we risk either under- or overestimating the hazard based on whether that particular displacement range yields a slip rate that is slower or faster than the current rate of fault slip (i.e., is that fault currently experiencing an earthquake cluster or an earthquake lull). What is needed to more accurately constrain this most basic input parameter for PSHA are many more incremental slip-rate data sets like the one we document in this paper. Such records from many more faults of different kinematics in different tectonic settings will be necessary to develop statistically meaningful ranges on the input parameters used in next generation PSHA to ensure more accurate estimation of future earthquake recurrence probabilities.

5 Conclusions

The new and revised slip rates presented here bolster and refine the previously sparse record of slip during mid-to-early Holocene time on the Garlock fault, providing a more nuanced view of the behavior of this fault than that suggested by previous results. Specifically, the new Summit Range East site data suggest that the fault did slip, albeit slowly, within the ~3300-year apparent seismic lull documented in earlier studies between 2.0 and 5.3 ka. Thus, earthquakes were occurring at a lower frequency or less elastic strain energy was released per event during this "slow" period, rather than one subsystem switching "off" entirely. As shown in this example, combining detailed incremental slip histories with paleo-earthquake age and displacement data, and geodetic measurements, provides insights into the behavior of major strike-slip faults, with implications for seismic hazard assessment and the geodynamics controlling strain accumulation and release in the upper crust across the complex plate boundary fault network in southern California. By documenting these factor of two to five-fold temporal variations in slip rate for the Garlock fault, we can significantly improve our understanding of the manner in which relative plate motions are accommodated through time in southern California.

Acknowledgements

This research was funded by U.S. National Science Foundation grants EAR-1650377 (Dolan) and EAR-1650364 (McGill). We thank James Hollingsworth, Alex Hatem, Rob Zinke, Lee McAuliffe, Plamen Ganev, Jessica Grenader, and CSUSB's 2016 Neotectonics class for their help gathering data for the Garlock fault. Additionally, we thank Rob Zinke for his help in using his RISeR formulation for calculating the incremental slip rates reported in this study. Thank you to Jonathan Griffin and the anonymous reviewer for their insightful comments.

Data and code availability

Supporting information for this article is available online. Slip rate calculations were performed using RISeR software (Zinke, 2021; Zinke et al., 2017, 2019).

Competing interests

The authors have no competing interests.

References

Andrew, J. E., Walker, J. D., and Monastero, F. C. Evolution of the central Garlock fault zone, California: A major sinistral fault embedded in a dextral plate margin. *Geological Society of America Bulletin*, 127(1–2):227–249, Aug. 2014. doi: 10.1130/b31027.1.

Berryman, K. R., Cochran, U. A., Clark, K. J., Biasi, G. P., Langridge, R. M., and Villamor, P. Major Earthquakes Occur Regularly on an Isolated Plate Boundary Fault. *Science*, 336(6089):1690–1693, June 2012. doi: 10.1126/science.1218959.

Blythe, A. and Longinotti, N. Exhumation of the southern Sierra Nevada–eastern Tehachapi Mountains constrained by low-temperature thermochronology: Implications for the initiation of the Garlock fault. *Lithosphere*, 5(3):321–327, June 2013. doi: 10.1130/l252.1.

Bronk Ramsey, C. Bayesian analysis of radiocarbon dates. *Radiocarbon*, 51(5), 2009. doi: 10.1017/S0033822200033865.

Burbank, D. W. and Whistler, D. P. Temporally constrained tectonic rotations derived from magnetostratigiraphic data: Implications for the initiation of the Garlock fault, California. *Geology*, 15(12):1172, 1987. doi: 10.1130/0091-7613(1987)15<1172:tctrdf>2.0.co;2.

Carter, B. Neogene offsets and displacement rates, central Garlock fault, California. In McGill, S. and Ross, T., editors, *Geological investigations of an active margin: Geological Society of America, Cordilleran Section Annual Meeting Guidebook*, volume v. 27, page 348–356, 1994.

Chuang, R. Y. and Johnson, K. M. Reconciling geologic and geodetic model fault slip-rate discrepancies in Southern California: Consideration of nonsteady mantle flow and lower crustal fault creep. *Geology*, 39(7):627–630, July 2011. doi: 10.1130/g32120.1.

Clark, M. Map showing recently active breaks along the Garlock and associated faults, California. *United States Geologic Survey Report*, (741), 1973. doi: 10.3133/i741.

Clark, M. and Lajoie, K. Holocene behavior of the Garlock fault. *Geological Society of America Abstracts with Programs*, 6(7): 156–157, 1974.

Davis, G. A. and Burchfiel, B. C. Garlock Fault: An Intracontinental Transform Structure, Southern California. *Geological Society of America Bulletin*, 84(4):1407, 1973. doi: 10.1130/0016-7606(1973)84<1407:gfaits>2.0.co;2.

Dawson, T. E., McGill, S. F., and Rockwell, T. K. Irregular recurrence of paleoearthquakes along the central Garlock fault near El Paso Peaks, California. *Journal of Geophysical Research: Solid Earth*, 108(B7), July 2003. doi: 10.1029/2001jb001744.

Del Vecchio, J., Lang, K. A., Robins, C. R., McGuire, C. P., and Rhodes, E. J. Storage and weathering of landslide debris in the eastern San Gabriel Mountains, California, USA: Implications for mountain solute flux. *Earth Surface Processes and Landforms*, 43(13):2724–2737, July 2018. doi: 10.1002/esp.4427.

Dolan, J. F., Bowman, D. D., and Sammis, C. G. Long-range and long-term fault interactions in Southern California. *Geology*, 35 (9):855, 2007. doi: 10.1130/g23789a.1.

Dolan, J. F., McAuliffe, L. J., Rhodes, E. J., McGill, S. F., and Zinke, R. Extreme multi-millennial slip rate variations on the Garlock fault, California: Strain super-cycles, potentially time-variable fault strength, and implications for system-level earthquake occurrence. *Earth and Planetary Science Letters*, 446:123–136, July 2016. doi: 10.1016/j.epsl.2016.04.011.

Evans, E. L. Persistent slip rate discrepancies in the eastern California (USA) shear zone: Reply. *Geology*, 45(9):e426–e426, Sept. 2017a. doi: 10.1130/g39439y.1.

Evans, E. L. A Comprehensive Analysis of Geodetic Slip-Rate Estimates and Uncertainties in California. *Bulletin of the Seismological Society of America*, 108(1):1–18, Nov. 2017b. doi: 10.1785/0120170159.

Evans, E. L., Thatcher, W. R., Pollitz, F. F., and Murray, J. R. Persistent slip rate discrepancies in the eastern California (USA) shear zone. *Geology*, 44(9):691–694, July 2016. doi: 10.1130/g37967.1.

Field, E. H., Biasi, G. P., Bird, P., Dawson, T. E., Felzer, K. R., Jackson, D. D., Johnson, K. M., Jordan, T. H., Madden, C., Michael, A. J., Milner, K. R., Page, M. T., Parsons, T., Powers, P. M., Shaw,

B. E., Thatcher, W. R., Weldon, R. J., and Zeng, Y. Long-Term Time-Dependent Probabilities for the Third Uniform California Earthquake Rupture Forecast (UCERF3). *Bulletin of the Seismological Society of America*, 105(2A):511–543, Mar. 2015. doi: 10.1785/0120140093.

Field, E. H., Jordan, T. H., Page, M. T., Milner, K. R., Shaw, B. E., Dawson, T. E., Biasi, G. P., Parsons, T., Hardebeck, J. L., Michael, A. J., Weldon, R. J., Powers, P. M., Johnson, K. M., Zeng, Y., Felzer, K. R., Elst, N. v. d., Madden, C., Arrowsmith, R., Werner, M. J., and Thatcher, W. R. A Synoptic View of the Third Uniform California Earthquake Rupture Forecast (UCERF3). *Seismological Research Letters*, 88(5):1259–1267, July 2017. doi: 10.1785/0220170045.

Friedrich, A. M., Lee, J., Wernicke, B. P., and Sieh, K. Geologic context of geodetic data across a Basin and Range normal fault, Crescent Valley, Nevada. *Tectonics*, 23(2), Apr. 2004. doi: 10.1029/2003tc001528.

Gan, W., Svarc, J. L., Savage, J. C., and Prescott, W. H. Strain accumulation across the Eastern California Shear Zone at latitude 36°30′N. *Journal of Geophysical Research: Solid Earth*, 105(B7): 16229–16236, July 2000. doi: 10.1029/2000jb900105.

Ganev, P. N., Dolan, J. F., McGill, S. F., and Frankel, K. L. Constancy of geologic slip rate along the central Garlock fault: Implications for strain accumulation and release in southern California. *Geophysical Journal International*, 190(2):745–760, May 2012. doi: 10.1111/j.1365-246x.2012.05494.x.

Garfunkel, Z. Model for the Late Cenozoic Tectonic History of the Mojave Desert, California, and for Its Relation to Adjacent Regions. *Geological Society of America Bulletin*, 85(12):1931, 1974. doi: 10.1130/0016-7606(1974)85<1931:mftlct>2.0.co;2.

Gauriau, J. and Dolan, J. Comparison of geodetic slip-deficit and geologic fault slip rates reveals that variability of elastic strain accumulation and release rates on strike-slip faults is controlled by the relative structural complexity of plate-boundary fault systems. *Seismica*, 3(1), Feb. 2024. doi: 10.26443/seismica.v3i1.1119.

Gauriau, J. and Dolan, J. F. Relative Structural Complexity of Plate-Boundary Fault Systems Controls Incremental Slip-Rate Behavior of Major Strike-Slip Faults. *Geochemistry, Geophysics, Geosystems*, 22(11), Nov. 2021. doi: 10.1029/2021gc009938.

Gold, R. D. and Cowgill, E. Deriving fault-slip histories to test for secular variation in slip, with examples from the Kunlun and Awatere faults. *Earth and Planetary Science Letters*, 301(1–2): 52–64, Jan. 2011. doi: 10.1016/j.epsl.2010.10.011.

Gold, R. D., Cowgill, E., Arrowsmith, J. R., Chen, X., Sharp, W. D., Cooper, K. M., and Wang, X.-F. Faulted terrace risers place new constraints on the late Quaternary slip rate for the central Altyn Tagh fault, northwest Tibet. *Geological Society of America Bulletin*, 123(5–6):958–978, Jan. 2011. doi: 10.1130/b30207.1.

Griffin, J. D., Stirling, M. W., Wilcken, K. M., and Barrell, D. J. A. Late Quaternary Slip Rates for the Hyde and Dunstan Faults, Southern New Zealand: Implications for Strain Migration in a Slowly Deforming Continental Plate Margin. *Tectonics*, 41(9), Sept. 2022. doi: 10.1029/2022tc007250.

Guest, B., Pavlis, T. L., Golding, H., and Serpa, L. Chasing the Garlock: A study of tectonic response to vertical axis rotation. *Geology*, 31(6):553, 2003. doi: 10.1130/0091-7613(2003)031<0553:ctgaso>2.0.co;2.

Harvey, A. M. and Wells, S. G. *Late Quaternary variations in alluvial fan sedimentologic and geomorphic processes, Soda Lake basin, eastern Mojave Desert, California*. Geological Society of America, 2003. doi: 10.1130/0-8137-2368-x.207.

Hatem, A. E. and Dolan, J. F. A Model for the Initiation, Evolution, and Controls on Seismic Behavior of the Garlock Fault, California. *Geochemistry, Geophysics, Geosystems*, 19(7):2166–2178, July 2018. doi: 10.1029/2017gc007349.

Hatem, A. E., Dolan, J. F., Zinke, R. W., Langridge, R. M., McGuire, C. P., Rhodes, E. J., Brown, N., and Van Dissen, R. J. Holocene to latest Pleistocene incremental slip rates from the east-central Hope fault (Conway segment) at Hossack Station, Marlborough fault system, South Island, New Zealand: Towards a dated path of earthquake slip along a plate boundary fault. *Geosphere*, 16 (6):1558–1584, Oct. 2020. doi: 10.1130/ges02263.1.

Hearn, E. "Ghost Transient" Corrections to the Southern California GPS Velocity Field from San Andreas Fault Seismic Cycle Models. *Seismological Research Letters*, 93(6):2973–2989, Aug. 2022. doi: 10.1785/0220220156.

Hearn, E. H., Pollitz, F. F., Thatcher, W. R., and Onishi, C. T. How do "ghost transients" from past earthquakes affect GPS slip rate estimates on southern California faults? *Geochemistry, Geophysics, Geosystems*, 14(4):828–838, Apr. 2013. doi: 10.1002/ggge.20080.

Kirby, M. E., Heusser, L., Scholz, C., Ramezan, R., Anderson, M. A., Markle, B., Rhodes, E., Glover, K. C., Fantozzi, J., Hiner, C., Price, B., and Rangel, H. A late Wisconsin (32–10k cal a BP) history of pluvials, droughts and vegetation in the Pacific south-west United States (Lake Elsinore, CA). *Journal of Quaternary Science*, 33(2):238–254, Feb. 2018. doi: 10.1002/jqs.3018.

Kozacı, Ö., Dolan, J. F., and Finkel, R. C. A late Holocene slip rate for the central North Anatolian fault, at Tahtaköprü, Turkey, from cosmogenic 10Be geochronology: Implications for fault loading and strain release rates. *Journal of Geophysical Research: Solid Earth*, 114(B1), Jan. 2009. doi: 10.1029/2008jb005760.

Loomis, D. P. and Burbank, D. W. The stratigraphic evolution of the El Paso basin, southern California: Implications for the Miocene development of the Garlock fault and uplift of the Sierra Nevada. *Geological Society of America Bulletin*, 100(1):12–28, Jan. 1988. doi: 10.1130/0016-7606(1988)100<0012:tseote>2.3.co;2.

Madden Madugo, C., Dolan, J. F., and Hartleb, R. D. New Paleoearthquake Ages from the Western Garlock Fault: Implications for Regional Earthquake Occurrence in Southern California. *Bulletin of the Seismological Society of America*, 102(6):2282–2299, Dec. 2012. doi: 10.1785/0120110310.

McClusky, S. C., Bjornstad, S. C., Hager, B. H., King, R. W., Meade, B. J., Miller, M. M., Monastero, F. C., and Souter, B. J. Present day kinematics of the Eastern California Shear Zone from a geodetically constrained block model. *Geophysical Research Letters*, 28 (17):3369–3372, Sept. 2001. doi: 10.1029/2001gl013091.

McGill, S. *Paleoseismology and neotectonics of the central and eastern Garlock fault, California*. [doctoral dissertation]„ California Institute of Technology, 1992.

McGill, S. and Rockwell, T. Ages of Late Holocene earthquakes on the central Garlock fault near El Paso Peaks, California. *Journal of Geophysical Research: Solid Earth*, 103(B4):7265–7279, Apr. 1998. doi: 10.1029/97jb02129.

McGill, S. and Sieh, K. Holocene slip rate of the Central Garlock Fault in southeastern Searles Valley, California. *Journal of Geophysical Research: Solid Earth*, 98(B8):14217–14231, Aug. 1993. doi: 10.1029/93jb00442.

McGill, S. F. and Sieh, K. Surficial offsets on the Central and Eastern Garlock Fault associated with prehistoric earthquakes. *Journal of Geophysical Research: Solid Earth*, 96(B13):21597–21621, Dec. 1991. doi: 10.1029/91jb02030.

McGill, S. F., Wells, S. G., Fortner, S. K., Kuzma, H. A., and McGill, J. D. Slip rate of the western Garlock fault, at Clark Wash, near Lone Tree Canyon, Mojave Desert, California. *Geological Society of America Bulletin*, 121(3–4):536–554, Feb. 2009. doi: 10.1130/b26123.1.

Meade, B. J. and Hager, B. H. Block models of crustal motion in southern California constrained by GPS measurements. *Journal of Geophysical Research: Solid Earth*, 110(B3), Mar. 2005. doi: 10.1029/2004jb003209.

Miller, M. M., Johnson, D. J., Dixon, T. H., and Dokka, R. K. Refined kinematics of the eastern California shear zone from GPS observations, 1993–1998. *Journal of Geophysical Research: Solid Earth*, 106(B2):2245–2263, Feb. 2001. doi: 10.1029/2000jb900328.

Monastero, F. C., Sabin, A. E., and Walker, J. D. Evidence for post-early Miocene initiation of movement on the Garlock fault from offset of the Cudahy Camp Formation, east-central California. *Geology*, 25(3):247, 1997. doi: 10.1130/0091-7613(1997)025<0247:efpemi>2.3.co;2.

Moulin, A. and Cowgill, E. The Mojave Section of the San Andreas Fault (California), 2: Pleistocene Records of Near-Field Transpression Illuminate the Atypical Evolution of the Restraining "Big Bend". *Geochemistry, Geophysics, Geosystems*, 24(10), Oct. 2023. doi: 10.1029/2023gc010897.

Ninis, D., Little, T. A., Van Dissen, R. J., Litchfield, N. J., Smith, E. G. C., Wang, N., Rieser, U., and Mark Henderson, C. Slip Rate on the Wellington Fault, New Zealand, during the Late Quaternary: Evidence for Variable Slip during the Holocene. *Bulletin of the Seismological Society of America*, 103(1):559–579, Feb. 2013. doi: 10.1785/0120120162.

Noriega, G., Arrowsmith, J., Grant, L., and Young, J. Stream Channel Offset and Late Holocene Slip Rate of the San Andreas Fault at the Van Matre Ranch Site, Carrizo Plain, California. *Bulletin of the Seismological Society of America*, 96(1):33–47, Feb. 2006. doi: 10.1785/0120050094.

Onderdonk, N. W., McGill, S. F., and Rockwell, T. K. Short-term variations in slip rate and size of prehistoric earthquakes during the past 2000 years on the northern San Jacinto fault zone, a major plate-boundary structure in southern California. *Lithosphere*, 7 (3):211–234, Feb. 2015. doi: 10.1130/l393.1.

Owen, L. A., Frankel, K. L., Knott, J. R., Reynhout, S., Finkel, R. C., Dolan, J. F., and Lee, J. Beryllium-10 terrestrial cosmogenic nuclide surface exposure dating of Quaternary landforms in Death Valley. *Geomorphology*, 125(4):541–557, Feb. 2011. doi: 10.1016/j.geomorph.2010.10.024.

Peltzer, G., Crampé, F., Hensley, S., and Rosen, P. Transient strain accumulation and fault interaction in the Eastern California shear zone. *Geology*, 29(11):975, 2001. doi: 10.1130/0091-7613(2001)029<0975:tsaafi>2.0.co;2.

Pena, K. Paleoseismology of the central Garlock fault in Searles Valley. Master's thesis, California State University, San Bernardino, 2019.

Platt, J. P. and Becker, T. W. Kinematics of rotating panels of E–W faults in the San Andreas system: what can we tell from geodesy? *Geophysical Journal International*, 194(3):1295–1301, June 2013. doi: 10.1093/gji/ggt189.

Reimer, P. J., Austin, W. E. N., Bard, E., Bayliss, A., Blackwell, P. G., Bronk Ramsey, C., Butzin, M., Cheng, H., Edwards, R. L., Friedrich, M., Grootes, P. M., Guilderson, T. P., Hajdas, I., Heaton, T. J., Hogg, A. G., Hughen, K. A., Kromer, B., Manning, S. W., Muscheler, R., Palmer, J. G., Pearson, C., van der Plicht, J., Reimer, R. W., Richards, D. A., Scott, E. M., Southon, J. R., Turney, C. S. M., Wacker, L., Adolphi, F., Büntgen, U., Capano, M., Fahrni, S. M., Fogtmann-Schulz, A., Friedrich, R., Köhler, P., Kudsk, S., Miyake, F., Olsen, J., Reinig, F., Sakamoto, M., Sookdeo, A., and Talamo, S. The IntCal20 Northern Hemisphere Radiocarbon Age Calibration Curve (0–55 cal kBP). *Radiocarbon*, 62(4):725–757, Aug. 2020. doi: 10.1017/rdc.2020.41.

Rhodes, E. J. Dating sediments using potassium feldspar single-grain IRSL: Initial methodological considerations. *Quaternary International*, 362:14–22, Mar. 2015. doi: 10.1016/j.quaint.2014.12.012.

Rittase, W. M., Kirby, E., McDonald, E., Walker, J. D., Gosse, J., Spencer, J. Q., and Herrs, A. Temporal variations in Holocene slip rate along the central Garlock fault, Pilot Knob Valley, California. *Lithosphere*, 6(1):48–58, Feb. 2014. doi: 10.1130/l286.1.

Saha, S., Moon, S., Brown, N. D., Rhodes, E. J., Scharer, K. M., McPhillips, D., McGill, S. F., and Castillo, B. A. Holocene Depositional History Inferred From Single-Grain Luminescence Ages in Southern California, North America. *Geophysical Research Letters*, 48(15), Aug. 2021. doi: 10.1029/2021gl092774.

Salisbury, J. B., Arrowsmith, J. R., Brown, N., Rockwell, T., Akciz, S., and Ludwig, L. G. The Age and Origin of Small Offsets at Van Matre Ranch along the San Andreas Fault in the Carrizo Plain, California. *Bulletin of the Seismological Society of America*, 108 (2):639–653, Jan. 2018. doi: 10.1785/0120170162.

Savage, J. C., Prescott, W. H., Lisowski, M., and King, N. E. Strain accumulation in southern California, 1973–1980. *Journal of Geophysical Research: Solid Earth*, 86(B8):6991–7001, Aug. 1981. doi: 10.1029/jb086ib08p06991.

Savage, J. C., Lisowski, M., and Prescott, W. H. An apparent shear zone trending north-northwest across the Mojave Desert into Owens Valley, eastern California. *Geophysical Research Letters*, 17(12):2113–2116, Nov. 1990. doi: 10.1029/gl017i012p02113.

Savage, J. C., Gan, W., and Svarc, J. L. Strain accumulation and rotation in the Eastern California Shear Zone. *Journal of Geophysical Research: Solid Earth*, 106(B10):21995–22007, Oct. 2001. doi: 10.1029/2000jb000127.

Smith, G. and Ketner, K. Lateral displacement on the Garlock fault, southeastern California, suggested by offset sections of similar metasedimentary rocks. *United States Geological Survey Professional Paper*, 700, 1970.

Smith, G. I. Large Lateral Displacement on Garlock Fault, California, as Measured from Offset Dike Swarm. *AAPG Bulletin*, 46, 1962. doi: 10.1306/bc74375f-16be-11d7-8645000102c1865d.

Smith, G. I. *Geology and volcanic petrology of the Lava Mountains, San Bernardino County, California*. 1964. doi: 10.3133/pp457.

US Geological Survey and California Geological Survey. Quaternary fault and fold database for the United States, 2023. https://www.usgs.gov/natural-hazards/earthquake-hazards/faults.

Van Dissen, R., Abbott, E., Zinke, R., Ninis, D., Dolan, J., Little, T., Rhodes, E., Litchfield, N., and Hatem, A. Slip rate variations on major strike-slip faults in central New Zealand and potential impacts on hazard estimation, 2020. https://repo.nzsee.org.nz/handle/nzsee/1691.

Wallace, R. Grouping and migration of surface faulting and variations in slip rates on faults in the Great Basin province. *Bulletin of the Seismological Society of America*, 77(3):868–876, 1987. doi: 10.1785/BSSA0770030868.

Weldon, R., Scharer, K., Fumal, T., and Biasi, G. Wrightwood and the earthquake cycle: What a long recurrence record tells us about how faults work. *GSA Today*, 14(9):4, 2004. doi: 10.1130/1052-5173(2004)014<4:watecw>2.0.co;2.

Zinke, R. rzinke/RISeR: RISeR full release (v1.0), 2021. doi: 10.5281/zenodo.4733235.

Zinke, R., Dolan, J. F., Rhodes, E. J., Van Dissen, R., and McGuire, C. P. Highly Variable Latest Pleistocene-Holocene Incremental Slip Rates on the Awatere Fault at Saxton River, South Island, New Zealand, Revealed by Lidar Mapping and Luminescence Dating. *Geophysical Research Letters*, 44(22), Nov. 2017. doi: 10.1002/2017gl075048.

Zinke, R., Dolan, J. F., Rhodes, E. J., Van Dissen, R., McGuire, C. P.,

Hatem, A. E., Brown, N. D., and Langridge, R. M. Multimillennial Incremental Slip Rate Variability of the Clarence Fault at the Tophouse Road Site, Marlborough Fault System, New Zealand. *Geophysical Research Letters*, 46(2):717–725, Jan. 2019. doi: 10.1029/2018gl080688.

Zinke, R., Dolan, J. F., Rhodes, E. J., Van Dissen, R. J., Hatem, A. E., McGuire, C. P., Brown, N. D., and Grenader, J. R. Latest Pleistocene–Holocene Incremental Slip Rates of the Wairau Fault: Implications for Long-Distance and Long-Term Coordination of Faulting Between North and South Island, New Zealand. *Geochemistry, Geophysics, Geosystems*, 22(9), Sept. 2021. doi: 10.1029/2021gc009656.